

2021-06

# A NONLINEAR NUMERICAL MODELING OF ACTIVE LATERAL EARTH PRESSURE DISTRIBUTION AND DISPLACEMENT PATTERN OF A RIGID CANTILEVER RETAINING WALL

SAMUEL, SIMENEH

---

<http://ir.bdu.edu.et/handle/123456789/12582>

*Downloaded from DSpace Repository, DSpace Institution's institutional repository*



**BAHIRDAR UNIVERSITY**  
**BAHIRDAR INSTITUTE OF TECHNOLOGY**  
**SCHOOL OF GRADUATE STUDIES**  
**FACULTY OF CIVIL AND WATER RESOURCE ENGINEERING**  
**A NONLINEAR NUMERICAL MODELING OF ACTIVE LATERAL EARTH**  
**PRESSURE DISTRIBUTION AND DISPLACEMENT PATTERN OF A RIGID**  
**CANTILEVER RETAINING WALL**

**MSC. THESIS**

**By**

**SAMUEL SIMENEH**

A thesis submitted to the school of graduate studies of Bahirdar University in partial fulfilment of the requirements for the Degree of Masters of Science in Geotechnical Engineering.

**Advisor: Dr.Ing. Henok Fikre**

**June, 2021**

**BAHIR DAR UNIVERSITY  
BAHIR DAR INSTITUTE OF TECHNOLOGY  
SCHOOL OF GRADUATE STUDIES  
FACULTY CIVIL AND WATER RESOURCES ENGINEERING**


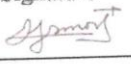

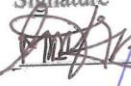
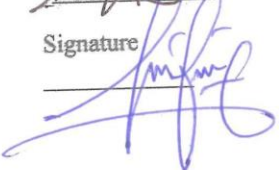
**Approval of thesis for defense result**

I hereby confirm that the changes required by the examiners have been carried out and incorporated in the final thesis.

Name of student: Samuel simeneh, Signature  date 13/08/2021

As members of the board of examiners, we examined this thesis entitled "a nonlinear numerical modeling of active lateral earth pressure distribution and displacement pattern of a rigid cantilever retaining wall" by Samuel Simeneh. We hereby certify that the thesis is accepted for fulfilling the requirements for the award of the degree of Masters of science in "Geotechnical Engineering".

**Board of Examiners**

Name of Advisor	Signature	Date
<u>Dr. Ing. Henok Fikre</u>		<u>09.08.21</u>
Name of External examiner	Signature	Date
<u>Dr. Africa Geremew</u>		<u>10.08.21</u>
Name of Internal Examiner	Signature	Date
<u>Dr. Binyam Bekele</u>	<u>Binyam Bekele</u>	<u>10/8/2021</u>
Name of Chairperson	Signature	Date
<u>Mr. Dagmawi Tesfaw</u>		<u>13/08/2021</u>
Name of Chair Holder	Signature	Date
<u>Mr. Melkamu Abebe</u>		<u>13/08/2021</u>
Name of Faculty Dean	Signature	Date
<u>Temesgen Enku Nigussie (PhD)</u> Faculty Dean		<u>Aug. 13, 2021</u>



## **Declaration**

This is to certify that the thesis entitled “a nonlinear numerical modeling of active lateral earth pressure distribution and displacement pattern of a rigid cantilever retaining wall”, submitted in partial fulfillment of the requirements for the degree of Master of Science in Geotechnical Engineering under Faculty of Civil and water Resources Engineering, Bahir Dar Institute of Technology, is a record of original work carried out by me and has never been submitted to this or any other institution to get any other degree or certificates. The assistance and help I received during the course of this investigation have been duly acknowledged.

Samuel Simeneh



13/08/2021

Name of the candidate

signature

Date

## Table of Contents

LIST OF FIGURES: .....	VII
LIST OF TABLES:.....	X
ABBREVIATIONS AND SYMBOLS.....	XI
ABSTRACT.....	XIII
ACKNOWLEDGEMENTS.....	XV
CHAPTER 1 .....	1
1. INTRODUCTION.....	1
1.1. Background .....	1
1.2. Problem Presentation.....	1
1.2. Scope of The Study .....	3
1.3. Objective of The Study .....	3
CHAPTER 2 .....	4
2. LITERATURE REVIEW.....	4
2.1. General .....	4
2.2. The Lateral Earth Pressure Problems .....	4
2.3. Lateral Earth Pressure Theories .....	4
2.4. Active Earth Pressure.....	8
2.5. Passive Earth Pressure.....	10
2.6. Previous Studies Related to Lateral Earth Pressure on Retaining Walls .....	11
2.7. Effect of Soil Arching on Lateral Soil Pressures .....	14
CHAPTER 3 .....	16
3. FINITE ELEMENT MODELING .....	16
3.1. Numerical Modelling Software.....	16
3.2. PLAXIS Model Setup .....	16

3.2.1. Initial and Boundary Conditions.....	16
3.3. Material Constitutive Model and Parameters.....	19
3.3.1 Soil Modelling.....	19
3.3.2 Modelling of Interface Element.....	27
3.3.3. Wall Modelling.....	29
3.3.4. Geometry of Wall.....	30
3.4. Validation.....	34
3.4.1. Hardening Soil Model Parameter Determination.....	35
3.5. Convergence Analyses.....	38
3.5.1 Mesh Sensitivity Analysis.....	38
3.5.2. Selection of Appropriate Finite Element Domain.....	40
CHAPTER 4.....	45
4. FINITE ELEMENT ANALYSIS RESULTS AND DISCUSSION.....	45
4.1. General.....	45
4.2. Soil Displacement.....	45
4.3. Wall Displacement.....	47
4.3.1 The Effect of Wall Dimensions on The Mode of Wall Displacement.....	48
4.3.4 The Effect of Base Width to Wall Height Ratio on Nodal Displacement of Point A ..	54
4.4. Determination of Lateral Pressure Distribution.....	57
4.4.1 The Effect of Wall Height on Lateral Earth Pressure Distribution Behind the wall Stem.....	57
4.4.1 The Effect of Base Width to Wall Height Ratio on Lateral Earth Pressure Distribution.....	60
4.4.2 Checking Arching Effect on Lateral Active Earth Pressure Distribution on The Wall Stem.....	62
CHAPTER 5.....	64

5.1. CONCLUSION ..... 64

Recommendations for Future Work..... 66

REFERENCES..... 67

## LIST OF FIGURES:

<b>Figure 2.1.</b> Graphical depictions of (a) Coulomb’s lateral active earth pressure theory (1776) (b) Rankine’s lateral active soil pressure theory (1857).....	5
<b>Figure 2.2.</b> Active and passive conditions for translating rigid retaining walls.....	6
<b>Figure 2.3</b> Nature of lateral earth pressure on a retaining wall (advanced foundation engineering-1 module 6 lecture 20). .....	7
<b>Figure 2.4.</b> An illustration of wall backfills interface (Ertuğrul, 2013). .....	8
<b>Figure 2.5.</b> Moher circle for different stress states. ....	10
<b>Figure 2.6.</b> Development of active and passive earth pressures. ....	11
<b>Figure 2.7</b> Shear failure in sand due to yield of lateral support by tilting about its upper edge. .	15
<b>Figure 3.1.</b> Model which shows fixities applied for boundary conditions, soil layer thickness, ground water level and initial conditions.....	17
<b>Figure 3.2.</b> Phases in PLAXIS model. ....	19
<b>Figure 3.3.</b> Hyperbolic stress-strain relation in primary loading for a standard drained tri-axial test (Schanz, Vermeer and Bonnier, 1999). .....	21
<b>Figure 3.4</b> Resulting strain curve for a standard drained triaxial test including dilatancy cut-off (Schanz, Vermeer and Bonnier, 1999).....	23
<b>Figure 3.5.</b> Definition of $E_{50ref}$ and $E_{urref}$ for drained tri-axial test results (Schanz, Vermeer and Bonnier, 1999).....	25
<b>Figure 3.6.</b> Definition of $E_{oedref}$ in oedometer test result (Schanz, Vermeer and Bonnier, 1999). .....	26
<b>Table 3.1:</b> Material properties for Backfill and Foundation soil.....	28
<b>Table 3.2:</b> Wall modelling parameters. ....	30
<b>Figure 3.7.</b> Typical geometry of walls. ....	31
<b>Figure 3.8.</b> Four-meter height wall (4MHW) section view. ....	32
<b>Figure 3.9.</b> Six-meter height wall (6MHW) section view.....	32
<b>Figure 3.10.</b> Nine-meter height wall (9MHW) section view. ....	33
<b>Table 3.3:</b> Designation of wall dimension with backfill sand.....	33
<b>Figure 3.11.</b> Illustration of surcharge load. ....	34



<b>Figure 3.12.</b> Detailed diagram of experimental setup of physical model test used for validation Rizwan Khan et al. 2016).....	35
<b>Table 3.4:</b> Input parameters of soil and wall for validation (data from Rizwan Khan et al. 2016). .....	36
<b>Table 3.5:</b> Material properties for backfill and foundation soil. ....	36
<b>Figure 3.13.</b> Validation of numerical lateral earth pressure results with experimental study.....	38
<b>Figure 3.14.</b> Mesh finesse option. ....	39
<b>Figure 3.15.</b> Mesh convergence with lateral pressure distribution. ....	40
<b>Figure 3.16.</b> Mesh which shows various boundary limit A and B for size sensitivity analysis...	41
<b>Figure 3.17.</b> Lateral displacement of wall tip at the end of Surcharge loading for all boundary cases. ....	42
<b>Figure 3.18.</b> Lateral pressure distribution on the wall stem at the end of surcharge loading. ....	42
<b>Figure 3.19.</b> Finite element mesh model used in this study. ....	43
<b>Figure 3.20.</b> 3D representation of PLAXIS model used in this study. ....	44
<b>Figure 4.1.</b> Typical deformed mesh shows how much the nodes in the mesh moves. ....	45
<b>Figure 4.2.</b> Total displacement vector of the soil representing the amount of soil displacement at the end of surcharge loading. ....	46
<b>Figure 4.3.</b> Total displacement vector of the wall shows direction and magnitude of displacement of the structure. ....	47
<b>Figure 4.4.</b> Nodal displacement pattern of the wall. ....	48
<b>Figure 4.5.</b> Total displacement of point B (B/H=0.4) considering different wall height.....	49
<b>Figure 4.6.</b> Total displacement of point B (B/H=0.5) considering different wall height.....	50
<b>Figure 4.7.</b> Total displacement of point B (B/H=0.6) considering different wall height.....	50
<b>Figure 4.8.</b> Total displacement of point B (B/H=0.7) considering different wall height.....	51
<b>Figure 4.9:</b> Effect of base width to stem height ratio on total displacement of nodal point B (at the stem bottom) 4 m height wall. ....	52
<b>Figure 4.10:</b> Effect of base width to stem height ratio on total displacement of nodal point B (at the stem bottom) 6 m height wall ....	53
<b>Figure 4.11:</b> Effect of base width to stem height ratio on total displacement of nodal point B (at the stem bottom) 9 m height wall ....	53

**Figure 4.12.** Effect of base width to stem height ratio on lateral displacement of nodal point A (at the stem top) for different wall height. **(a).** 4m height wall, **(b).** 6m height wall, **(c).** 9m height wall..... 56

**Figure 4.13.** Effect of wall height on lateral earth pressure distribution; (a). walls with B/H 0.4, (b). walls with B/H 0.5, (c). wall with B/H 0.6, and (d). walls with B/H 0.7..... 59

**Figure 4.14.** Effect of base width to height ratio on lateral earth pressure distribution, (a). lateral pressure variation for 4MHW, (b). lateral pressure variation for 6MHW, and (c). lateral pressure variation for 9MHW. .... 61

**Figure 4.15.** Lateral active earth pressure distribution with and without wall friction behind the stem. .... 63

**LIST OF TABLES:**

**Table 3.1:** Material properties for Backfill and Foundation soil..... 28

**Table 3.2:** Wall modelling parameters. .... 30

**Table 3.3:** Designation of wall dimension with backfill sand..... 33

**Table 3.4:** Input parameters of soil and wall for validation (data from Rizwan Khan et al. 2016).  
..... 36

**Table 3.5:** Material properties for backfill and foundation soil. .... 36

## ABBREVIATIONS AND SYMBOLS

4MHW	Four-meter height wall
6MHW	Six-meter height wall
9MHW	Nine-meter height wall
B	Base width of the wall footing
B/H	The ratio of base width to wall height
$c_{ref}$	Cohesion
$D_f$	Thickness of base width
$D_r$	Relative density
E	The elasticity(young's) modules in GP
$E_{50}^{ref}$	Secant stiffness in standard drained tri-axial test
$E_{oed}^{ref}$	Tangent stiffness for primary oedometer loading and
$E_{ur}^{ref}$	Unloading/reloading stiffness
$f_{ck}$	Characteristic cylinder comprehensive strength in MPa
$G_{ur}$	Elastic shear modulus
$K_0$	At rest earth pressure coefficient
$K_a$	Active earth pressure coefficient
$K_p$	Passive earth pressure coefficient
$L_t$	Projection of toe from the stem base
$m$	Power for stress-level dependency of stiffness
OCR	Over-consolidation ratio
POP	Pre-overburden pressure
$p^{ref}$	Reference stress for stiffness
$R_{inter}$	Interface reduction factor

$R_f$	Failure ratio $q_f/q_a$
$\nu_{ur}$	Poisson's ratio for unloading-reloading,
$\Phi$	Friction angle
$\Psi$	Dilatancy angle
$\nu_{ur}$	Poisson's ratio
$\sigma_3$	Minor principal stress
$\sigma_1$	Major principal stress
$\delta_a^{max}$	Wall displacement corresponding to the limit active state
$\delta_p^{max}$	Wall displacement corresponding to the limit passive state
$\delta_{ht}$	Horizontal movement of wall at the top of the stem
$\delta_{hb}$	Horizontal movement of wall at the bottom of the stem
$\delta_{hv}$	Vertical movement of wall at the bottom of the stem
$\gamma_{unsat}$	Unit weight above the phreatic level
$\gamma_{sat}$	Unit weight below the phreatic level

## **ABSTRACT**

In this study, the finite element method is used to investigate the variation and distribution nature of lateral earth pressure and displacement pattern behind a rigid cantilever wall. To provide resistance to overturning and sliding, the design of cantilever retaining wall starts by proportioning the wall dimension. Commonly, a limit equilibrium method is used to analyze the stability of the wall. However, the limit equilibrium method is unable to predict the displacement of the wall. In most design cases, a preliminary ratio between the base width and the wall height is assumed from 0.4 to 0.7 to ensure the stability requirement, however, there were variation in displacement pattern of the wall in terms of rotations and translations, and the lateral pressure profile. For the simulation of inverted T-shape wall which supports backfill sand PLAXIS 3D connect edition were used. The hardening soil model and linear elastic model, are used for modelling the soil and the retaining wall respectively. For validating the proposed numerical model reference was made to physical model test. Within the scope of the analysis, inverted T type cantilever retaining wall parameters such as the ratio of base width to wall height ranging from 0.4 to 0.7 for different wall height case considered. Considering the geometry, dimensions of the wall and the hardening soil model the predicted pattern and magnitude of wall displacement were discussed. Finally, the displacement pattern of wall, the nature of lateral earth pressure distribution acting on the wall stem and the slope of lateral pressure distribution line investigated for all the walls with 4 m, 6 m and 9m heights.

Wall with smaller base width develops active earth pressure with in higher displacement limit and wall with larger base width develops active earth pressure in smaller displacement limit. For the value of base width to wall height ratio less than or equal to 0.5 the rotational effect of displacement

pattern dominant. However, for the value of base width to wall height ratio greater than and equal to 0.6 the translational effect of displacement pattern governs.

**Keywords:** Numerical model, Plaxis program, Lateral earth pressure, Wall displacement, Proportioning.

## **Acknowledgements**

I wish to express my sincere gratitude to my advisor Dr.Ing. Henok Fikre for providing me an opportunity to do my thesis paper in the specified topic and for his precious assistance in all of this research work. I am sincerely thankful for his valuable encouragement, direction, advice and helpful contribution during the preparation of this work.

I also thank the chairholder of Bahirdar institute of technology geotechnical engineering department Mr. Melkamu Abebe for providing me the opportunity to embark on this paper



# CHAPTER 1

## 1. INTRODUCTION

### 1.1. Background

The calculation of lateral earth pressures on soil retaining walls induced by granular backfill and surcharge loads is one of the oldest problems of soil mechanics. Coulomb's (1776) and Rankine's (1857) theories, which are based on limit equilibrium techniques are extensively used to calculate the lateral soil pressures acting on soil retaining walls. Accurate estimation of lateral earth pressure is essential in geotechnical engineering, especially in the design of retaining wall. Hence, these retaining walls are used to provide lateral resistance for a mass of earth or other material to accommodate a transportation facility. These walls are used in a variety of applications including right-of-way restrictions, protection of existing structures that must remain in place, grade separations, new highway embankment construction, roadway widening, stabilization of slopes, protection of environmentally sensitive areas, staging, and temporary support including excavation or underwater construction support, etc. Safe and economical design of retaining structures requires a sound knowledge of the contact pressure exerted against them. An accurate distribution of lateral earth pressure enables an efficient design of retaining wall which reduces the chance of over or under design of the walls. An overdesign of a retaining wall will lead to wastage of construction materials whereas an under design will lead to a higher risk of failure. When Rankin or Coulomb theories are used to design of retaining wall, it is accepted beforehand that the retaining wall will experience a lateral displacement (as cited in Medina, Sau and Quintana, 2016). This displacement is normally not calculated when a retaining wall is designed. In present study, numerical modeling using PLAXIS 3D conducted to predict this displacement.

### 1.2. Problem Presentation

The problem consists cantilever retaining wall with the shape of inverted T-type. The design of T-shaped cantilever retaining wall and support system requires careful analysis especially the

geometry of the wall. The design starts by proportioning the wall dimension for which stability is checked for. Commonly, limit equilibrium method (LEM) is used to analyse the performance, However, the LEM analysis is unable to predict the displacement of the wall. Thus, the numerical analysis using numerical finite element method (FEM) incorporated in PLAXIS 3D software computer program was adopted to analyze the behavior of T-shaped cantilever retaining wall. The nature of lateral earth pressure distribution, pattern and magnitude of displacement to reach the plastic equilibrium was conducted numerically, by many researchers (Rouili, Djerbib and Touahmia 2005; Rouili 2013) but they were considered only ‘‘L-shaped’’ retaining wall. Tang, Li and Yuan (2018), presents an analytical model which proposed to calculate earth pressure considering the displacement of gravity rigid wall, and this model is developed based on the hyperbolic soil stress-strain relationship. In comparison with numerical and experimental results, this analytical model can effectively predict the nonlinear earth pressure distribution with various modes of wall movement.

Sherif et al. 1984, Fang and Ishibashi 1986, Fang et al. 1994 study, laboratory modeling which has demonstrated that, earth pressure on a rigid retaining wall is affected by wall displacement and that the earth pressure distribution shows a nonlinear pattern under different modes of wall movement. From this experimental studies, the active earth pressures without enough wall displacements are larger than those corresponding to the limit state, while the passive earth pressure without accounting for the wall displacement may lead to an overestimation.

Kamiloglu and Sadoglu (2019) study, the effect of wall geometry on active failure surfaces and lateral earth pressure distribution on semi-gravity and cantilever walls using finite element method. From this finding Lateral earth pressure distribution varies based on retaining wall type. But the effect of wall geometry on displacement modes of wall does not considered.

In the present study, it is suggested to use PLAXIS 3D code in order to develop a numerical model, which is intended to predict the variation and distribution nature of lateral earth pressure behind a rigid cantilever retaining wall. The effect of base width to wall height ratio on displacement mode and the displacement pattern of inverted T-shaped wall which is not considered in previous studies were investigated. In most previous investigations, either pure rotation or translation was considered, but in present study the occurrence of both rotation and translation investigated. The

effect of arching on the distribution nature of active lateral pressure were checked from the computed numerical results.

## 1.2. Scope of The Study

Scope of the research is limited to analyze and study the nature of lateral earth pressure distribution, pattern and magnitude of wall displacement for cantilever inverted T-shaped retaining wall with height of 4m, 6m and 9m. Considering the described heights of wall the effect of proportioned base to wall height ratio ranging from 0.4 to 0.7 on the nature of earth pressure distribution and wall displacement pattern (mode of wall movement) and magnitude investigated.

For the simulation of stiff inverted T-shaped reinforced concrete cantilever retaining wall supporting sand, a numerical model was conducted using a finite element software program (PLAXIS 3D Connect Edition). The distribution of the earth pressure along the retaining wall height is compared to data obtained from previous physical modeling studies.

## 1.3. Objective of The Study

Here, the objectives of the research are summarized as follow;

1. Study the nonlinear nature of lateral earth pressure distribution at the back of inverted T type cantilever retaining wall backfilled with sand using the finite element software PLAXIS 3D.
2. Predicting pattern and magnitude of wall displacement, considering different wall heights and base widths.
3. Predict the lateral pressure profile and the distribution nature of lateral pressure for various wall dimensions.
4. Determining the mode of wall movement as *rotational* or *translational* for the considered wall dimension.
5. Check the effect of the variation of wall dimension on the displacement limit to develop active lateral earth pressure.

# CHAPTER 2

## 2. LITERATURE REVIEW

### 2.1. General

Determination of lateral earth pressure is one of the common problems in geotechnical engineering. Estimation of the active lateral earth pressures is very important in the design phase of the retaining walls, especially for earth retaining walls.

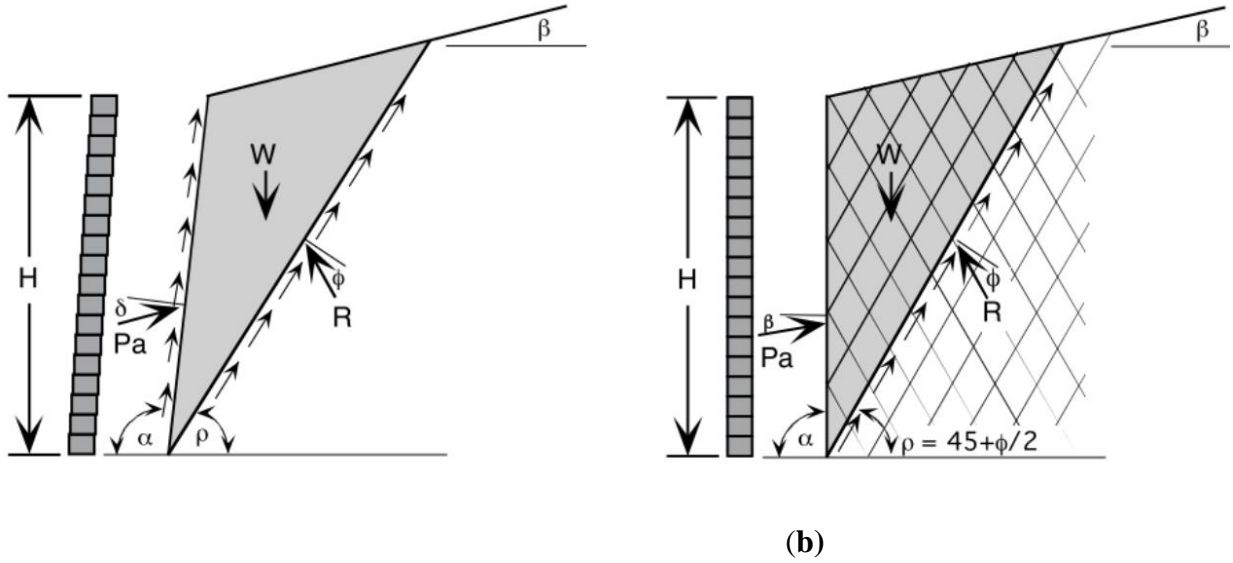
### 2.2. The Lateral Earth Pressure Problems

Lateral earth pressure is a significant design element in a number of foundation engineering problems. Retaining and sheet-pile walls, both braced and unbraced excavations, and earth or rock contacting tunnel walls and other underground structures require a quantitative estimate of the lateral pressure on a structural member for either a design or stability analysis. Earth pressures are developed during soil displacements (or strains) but until the soil is on the verge of failure. Rankine earth pressure theory states that a soil mass must strain some finite amount in order to mobilize either passive or active shear resistance. Rogers (1986) depicted that, the amount of this lateral strain is commonly in the range of  $0.002H$  (sand) to  $0.02H$  (clay) for the active range and  $0.005H$  (sand) to  $0.04H$  (clay) for the passive range, where  $H$  is equivalent to the total height of the wall including the buried portion.

### 2.3. Lateral Earth Pressure Theories

There are two commonly accepted theories for calculating lateral earth pressures, namely Coulomb's (1776) lateral earth pressure theory and Rankine's (1857) earth pressure theory. These theories are based on the common assumptions that the retained soil is homogeneous, isotropic, semi-infinite and well drained to avoid consideration of pore pressures. These assumptions lead to hydrostatic or triangular pressure distributions when calculating the lateral earth pressures being exerted against a vertical plane. The Coulomb theory is defined as an elastic-perfectly plastic model. Until the stress path has targeted the failure envelope, no plastic deformation follow.

However, Rankine considered soil in a state of plastic equilibrium and used essentially the same assumptions as Coulomb, he assumed no wall friction or soil cohesion. Graphical depictions of Coulomb's and Rankine's Theories are given in Figure 2.1.



**Figure 2.1.** Graphical depictions of (a) Coulomb's lateral active earth pressure theory (1776) (b) Rankine's lateral active soil pressure theory (1857)

*Coulomb's lateral active earth pressure;*

$$P_{ah} = \frac{\gamma H^2}{2} K_a \cos(\delta - (90 - \alpha)) \quad (2.1)$$

$$K_a = \frac{\sin^2(\alpha + \phi)}{\sin^2 \alpha \sin(\alpha - \delta) \left[ 1 + \frac{\sin(\phi + \delta) \sin(\phi - \beta)}{\sin(\phi - \delta) \sin(\phi + \beta)} \right]^2} \quad (2.2)$$

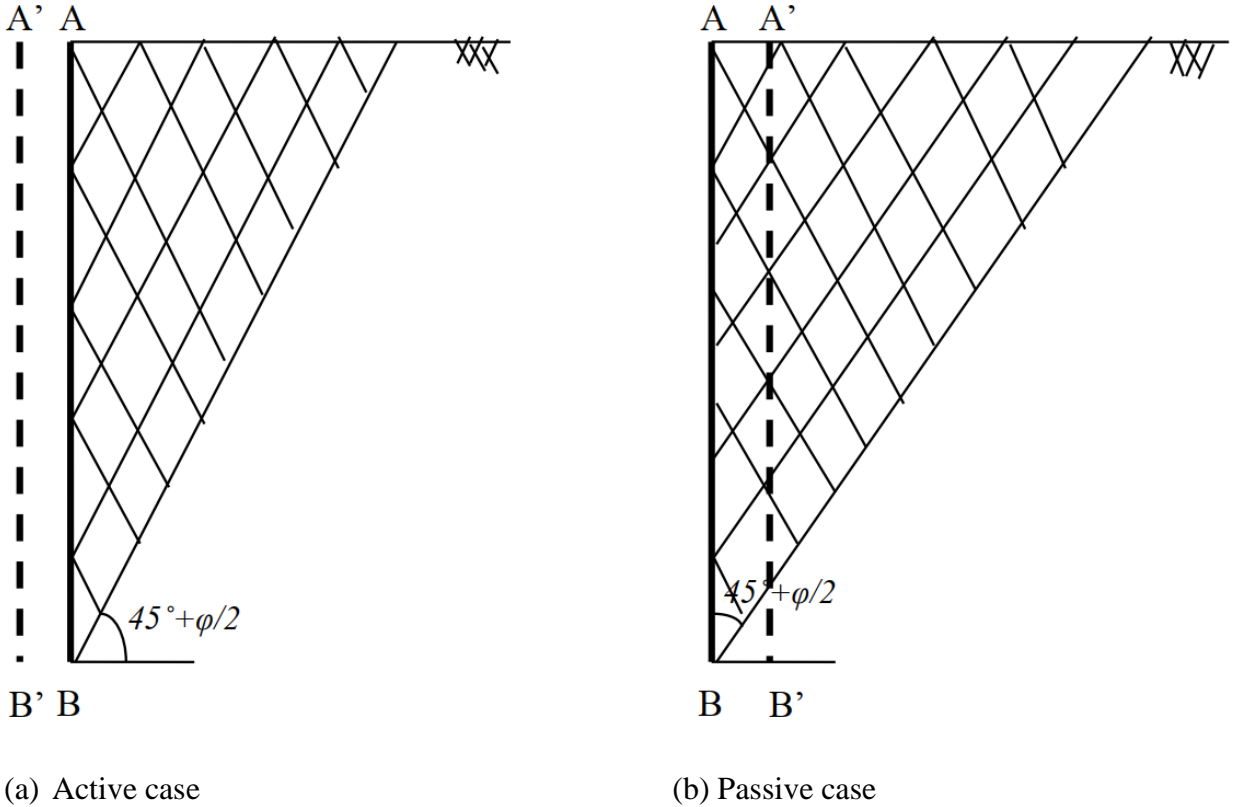
Where  $\alpha$  is the inclination of the wall in relation to the vertical,  $\beta$  the ground slope,  $\phi$  is the internal friction angle and  $\delta$  the inclination of the friction resultant between wall and soil.

*Rankine's lateral active soil pressure;*

$$P_{ah} = \frac{\gamma H^2}{2} K_a \cos(\beta) \quad (2.3)$$

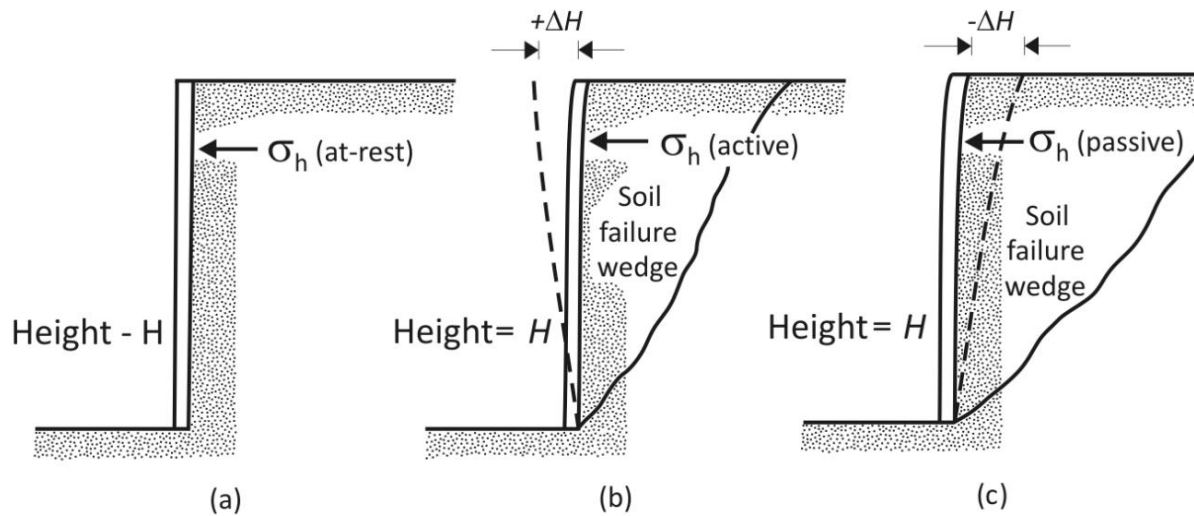
$$K_a = \cos \beta \frac{\cos \beta - \sqrt{\cos^2 \beta - \cos^2 \phi}}{\cos \beta + \sqrt{\cos^2 \beta - \cos^2 \phi}} \quad (2.4)$$

The theories of lateral earth pressure against retaining walls account for active and passive earth stresses. The active condition, generally resulting in the lowest earth pressures, occurs when the relative movement between the wall and the soil is away from each other. Figure 2.2 shows, the active and passive conditions for translating rigid earth retaining walls (Ertuğrul, 2013).



**Figure 2.2.** Active and passive conditions for translating rigid retaining walls.

Figure 2.3 shows, the nature of lateral earth pressure on a rotating retaining wall of height  $H$ . The wall may be restrained from moving (Figure 2.3a). The lateral earth pressure on the wall at any depth is called the at-rest earth pressure. The wall may tilt away from the soil retained (Figure 2.3b). With sufficient wall tilt, a triangular soil wedge behind the wall will fail. The lateral pressure for this condition is referred to as active earth pressure. The wall may be pushed into the soil retained (Figure 2.3c). With sufficient wall movement, a soil wedge will fail. The lateral pressure for this condition is referred to as passive earth pressure.



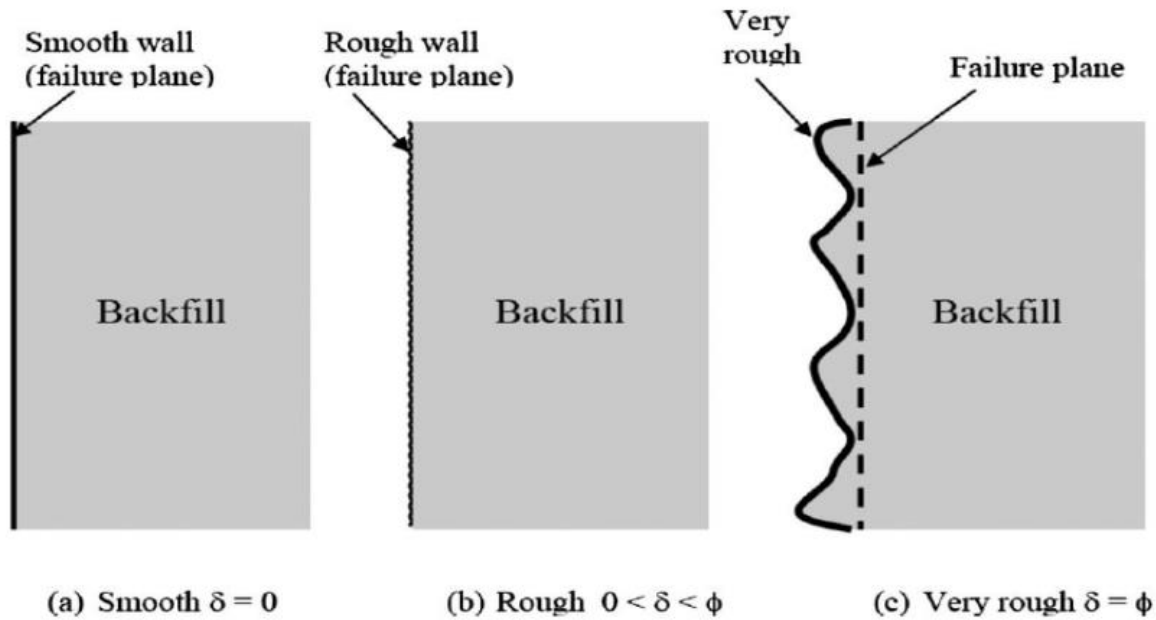
**Figure 2.3** Nature of lateral earth pressure on a retaining wall (advanced foundation engineering-1 module 6 lecture 20).

To achieve active state stress conditions within the backfill, the retaining wall undergoes flexural deformations, rotational (from the top or base), translational, and sliding type displacements. The amount of displacement required to reach active state is highly dependent upon the characteristics of the backfill soil and the displacement mode of the retaining wall (Ertuğrul, 2013). Lambe and Whitman addressed the shear strain requirement necessary to achieve active stress state as very little horizontal strain less than 0.5% of the retaining wall height.

Using identical parameters, the lateral load calculated from Coulomb's theory is less than the earth force calculated by Rankine's theory. It should be noticed that Coulomb's method is a graphical approach considering the equilibrium of the forces acting on the soil wedge and it does not have the ability to give information about the distribution of lateral stress along the wall height (Ertuğrul, 2013).

Additionally, Rankine's theory does not account for the soil-wall interface friction effect. In 2013, Ertuğrul depicted three possible modes of shear resistance along the wall-backfill interface. In Figure 2.4(a), a smooth wall condition is illustrated. According to this case, the retaining wall does not carry any shear stress since there is no wall backfill friction. In Figure 2.4(b), a rough wall condition is depicted. According to this condition, frictional forces occur along the wall-backfill

interface along which shear stress can be carried within the retained material by enabling lateral arching. In Figure 2.3(c), a very rough wall surface is depicted. This type of surface significantly increases the wall-backfill interface friction.



**Figure 2.4.** An illustration of wall backfills interface (Ertuğrul, 2013).

In the following sections we will discuss various relationships to determine the at-rest, active, and passive pressures on a retaining wall. It is assumed that the readers have been exposed to lateral earth pressure in the past, so this chapter will serve as a review.

## 2.4. Active Earth Pressure

The schematics of analytical model (Tang, Li and Yuan, 2018) shown in Figure 2.6 illustrates the change in the earth pressure with different wall movements. If the wall moves away from the soil mass, the lateral earth pressure is represented as the active case, and the corresponding wall displacement at depth  $z$  is  $\delta_a$ . If the wall moves against the soil mass,  $\delta_p$  indicates the wall displacement at depth  $z$  for the passive case. If the unit weight of soil is  $\gamma$ , the vertical stress in soils at depth  $z$  is always  $\gamma z$ , and the initial lateral earth pressure is  $K_0 \gamma z$ , where  $K_0$  is the coefficient of earth pressure at rest and can be determined using Jaky's equation (Craig 2004), Since  $K_0$  is less



than 1 for normally consolidated soils, the vertical stress at the initial state is the major principal stress  $\sigma_1$ , whereas the lateral earth pressure is the minor principal stress  $\sigma_3$ . The initial stress state (**State I**) can be represented as a Mohr circle, as shown in Figure. 2.5. If we consider the backfill is homogeneous then both  $\sigma_1$  and  $\sigma_3$  increase linearly with depth  $z$  in such a case the ratio of  $\sigma_3$  and  $\sigma_1$  remains constant with depth  $z$ , that is,

$$\frac{\sigma_3}{\sigma_1} = \frac{\sigma_3}{\gamma z} = \text{constant} = K_0 \quad (2.5)$$

Where  $K_0$  is the coefficient of at rest earth pressure.

The lateral earth pressure  $\sigma_3$  acting on the wall at any depth  $z$  may expressed as

$$\sigma_3 = K_0 \gamma z \quad (2.6)$$

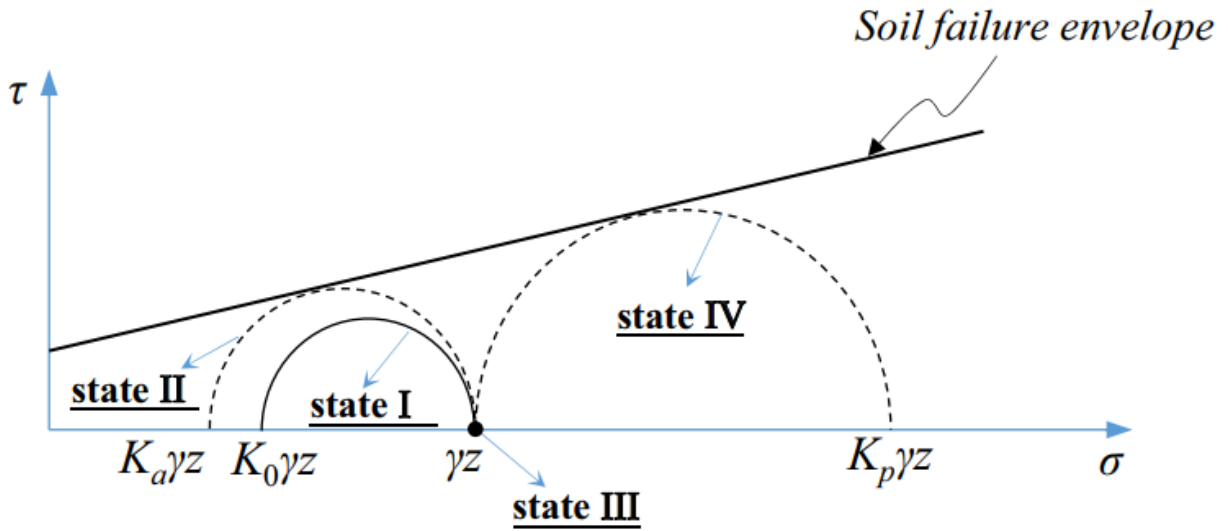
As shown in Figure 2.6, as the retaining wall moves away from the soil mass, the lateral earth pressure decreases, whereas the corresponding Mohr circle expands. If the wall displacement is sufficient, the lateral pressure reaches plastic equilibrium during this Mohr circle reaches the soil failure envelope, the earth pressure is the limit active earth pressure at State II with a coefficient  $K_a$ , indicating that the lateral earth pressure at depth  $z$  is  $K_a \gamma z$ . As shown in Figure 2.5, the required wall displacement to reach the limit active state is  $\delta_a^{max}$ . The minimum principal stress (Bowles, 1996, P. 590)  $\sigma_3$  termed as the active earth pressure and can be computed as

$$\sigma_3 = \sigma_1 \tan^2\left(45 - \frac{\phi}{2}\right) - 2c \tan\left(45 - \frac{\phi}{2}\right) \quad (2.7)$$

For cohesion less soil,

$$\sigma_3 = K_a \gamma z \quad (\text{since } c=0) \text{ where } K_a = 1 - \sin\phi \quad (2.8)$$

Since the wall must displace/rotate laterally away from the soil being retained to produce active (or  $K_a$ ) earth pressure conditions, the question is, how much rotation is necessary? Bowles (1996, P. 592), modestly investigate the displacement limit for cohesionless dense sand 0.001 to 0.002H and cohesion less loose sand 0.002 to 0.004H and these can be used as a guide.



**Figure 2.5.** Mohr circle for different stress states.

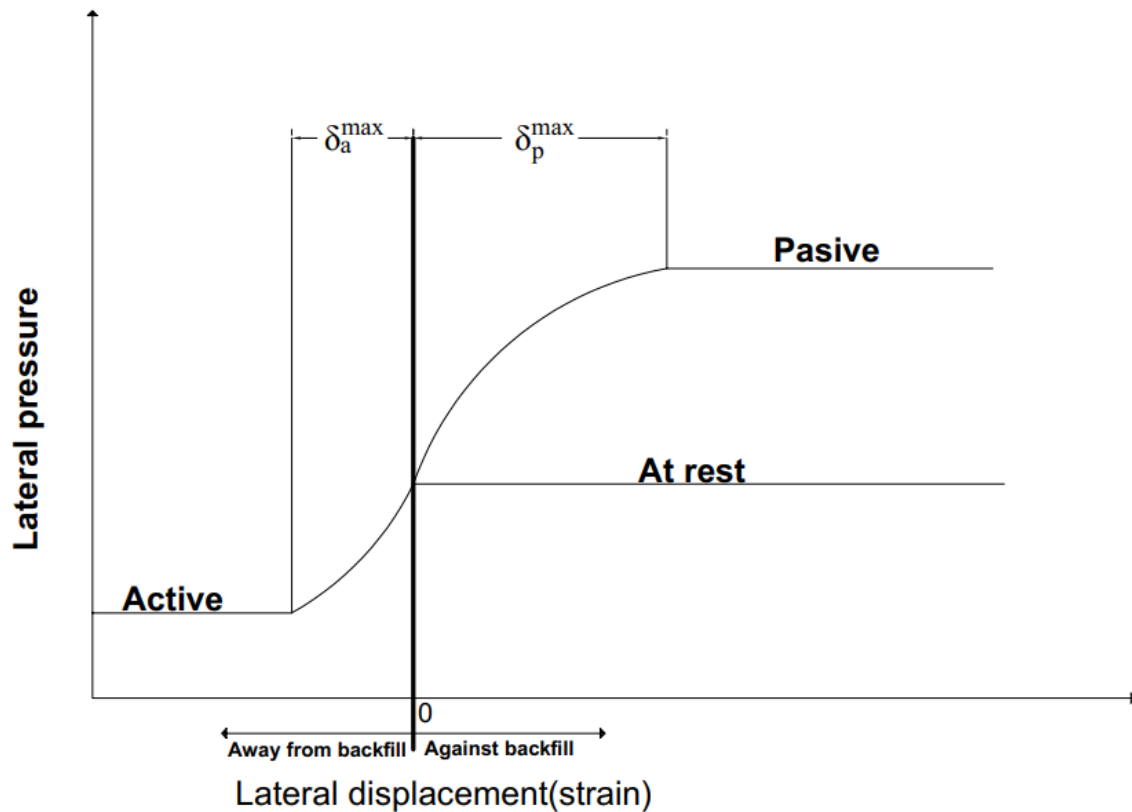
## 2.5. Passive Earth Pressure

If the wall moves against the soil mass,  $\delta_p$  indicates the wall displacement at depth  $z$  for the passive case. If the wall moves against the soil mass, the lateral earth pressure increases and can reach the limit passive earth pressure (**State IV**), at which point the lateral earth pressure at depth  $z$  is  $K_p \gamma z$ , where  $K_p$  is the passive earth pressure coefficient. The wall displacement corresponding to the limit passive state is  $\delta_p^{max}$ . At this state the vertical stress is the minor principal  $\sigma_3$  and the lateral earth pressure is the major principal stress  $\sigma_1$  and it can be computed as,

$$\sigma_1 = \sigma_3 \tan^2\left(45 + \frac{\phi}{2}\right) + 2c \tan\left(45 + \frac{\phi}{2}\right) \quad (2.9)$$

Mei et al. proposed that (as cited in Yao Tang et al. 2018) there exists a turning point of earth pressure variation as the wall moves against the soil mass, **State III** in Figure 2.5, and the lateral earth pressure is equal to the vertical stress at this turning point. In other words, the turning point is at the isotropic stress state.

Passive earth pressure developed by increasing the lateral pressure from **state III** to **State IV**. Again, the soil undergoes deformation and with sufficient deformation, the maximum shear resistance is mobilized.



**Figure 2.6.** Development of active and passive earth pressures.

## 2.6. Previous Studies Related to Lateral Earth Pressure on Retaining Walls

Various numerical analyses were conducted to predict the earth pressure accounting wall geometry and diminution. Kamiloğlu, Sadoglu and Yilmaz (2019) study the effect of wall geometry on active failure surface and lateral earth pressure distribution by considering gravity retaining wall and cantilever retaining wall with various heel lengths. In the investigation short heel and long heel cases play decisive role in lateral earth pressure distribution. Heel length is effective parameter for the walls with short heel. On the other hand, heel length has no effect on lateral earth pressure for the walls with long heel. Rouili (2013) presents the results of numerical analysis considering ratio

between the lengths of the base and the stem for cantilever L-shaped wall. The results show that the proportioning governs the equilibrium between the instantaneous rotation and the translation of the wall-toe, also, the lateral pressure estimation based on the average value between the at-rest and the active pressure, recommended by most design standards, is found to be not applicable for all walls. Rouili, Djerbib and Touahmia (2005) develops numerical model to simulate the behavior of a stiff “L” shaped retaining wall supporting sand and taking reference to an experimental model tested in a centrifuge experiment, it was found that the predicted pattern and magnitude of the wall displacements were close to the experimentally observed results. A good agreement between the measured and the numerically computed lateral pressures acting on the wall stem was also obtained with comparison to the classical approach.

Soon Poh and Shirazi (2012) proposed the comparative study of different theories on active earth pressure with finite element analysis using PLAXIS software. The comparative results showed that in terms of distribution and magnitude of active earth pressure, and they conclude that Rankine’s theory possesses highest match and compatible to the PLAXIS analysis among all other theories. While in parametric studies, when soil friction angle and wall friction increase, the active earth pressure decreases. On the other hand, when the soil unit weight and height of wall increase, the active earth pressure increases. Cheng and Yung (2010) investigated active earth pressure on rigid retaining wall built near rock faces using finite element method. The fill space behind the wall was limited due to the presence of the rock face. Rock faces behind the fill space with various sloping conditions and with various distance from the wall were taken into account in the finite element (FE) analyses. In addition, the effect of the aspect ratio of the fill space and the friction angle of the fill on the coefficient of active earth pressure and the location of the resultant of active earth pressure was also investigated. The coefficients ( $K_{a(c)}$ ) of the active earth pressure on rigid walls near rock faces were considerably less than the Coulomb solution and decreased with increasing inclination ( $\beta$ ) of the rock face if the stiff boundary was within the Rankine’s active wedge.

In 2003, Yildiz investigated the effects of the material parameters used to represent the stress-strain relationship of the soil, on lateral pressures due to surface strip loading. It is concluded that shear strength parameters (cohesion and angle of friction) of the soil are major effective parameters affecting lateral pressures which can be determined by conventional laboratory or in-situ tests. In

2013, Amer studied the effect of increasing wall penetration depth on the behavior of cantilever and anchored sheet pile walls for varying wall heights in different soil types using PLAXIS finite element software. The wall behavior was investigated through the wall displacements, bending moments, and anchor forces. The overall findings of the study indicate that increasing wall penetration depth has significant effect on the structural behavior of sheet pile walls. Increasing wall penetration depth can reduce the cantilever wall deformations significantly, and this can also yield a significant decrease in the wall bending moment for anchored sheet pile walls. Albusoda, Abbas and Awn (2017), develops numerical modeling of retaining wall resting on expansive soil. Retaining walls rested on expansive soils are subjected to uplift due to soil swelling. More importantly, the swelling in expansive soil tends to cause additional lateral pressure on wall that caused deformations and bending. Various pattern types of helical piles are used to reduce the vertical and lateral movement of retaining wall constructed on expansive soil. The backfill soil beyond retaining wall is affected by swelling of expansive soil that caused additional lateral earth pressure on the wall of retaining wall. From there study, the use of inclined helical piles beside vertical helical piles under the base of retaining wall decreased vertical movement 94% and lateral movement 70% for ratio of length of helical pile to depth of expansive soil ( $L/H$ ) equal to 3.2. In general, the presence of helical piles below retaining wall resisted and controlled the vertical movement but do not control lateral movement except the case of using inclined helical piles.

Various analytical models were proposed to predict the earth pressure accounting for the wall movement. Yao Tang et al. (2018) proposed an analytical model to calculate earth pressure considering the displacement of a rigid wall. Lateral displacement of retaining walls (Medina, Sau and Quintana, 2016) in the lateral displacement of a gravity retaining wall is presented. From the result it concludes that, when a retaining wall is designed, if the project permits, it is very convenient to design the wall so that it moves in a horizontal direction, decreasing the earth pressure on the active side and increasing the pressure of on the passive side, and therefore a more economic wall is obtained when lateral displacement is allowed. As the wall moves in the horizontal direction, the earth pressure decreases on the active side and increases on the passive side, so that the balance of forces in the horizontal direction is reached.

Sotto and Miliziano (2014) found that, in the design of retaining structures, where the structural element is modeled as a 1D beam element with young modulus,  $E$ , moment of inertia,  $I$ , and area,

A, of the real geometry. This approach often fails to predict the actual behavior of the soil structure system and overestimation of displacement can occur.

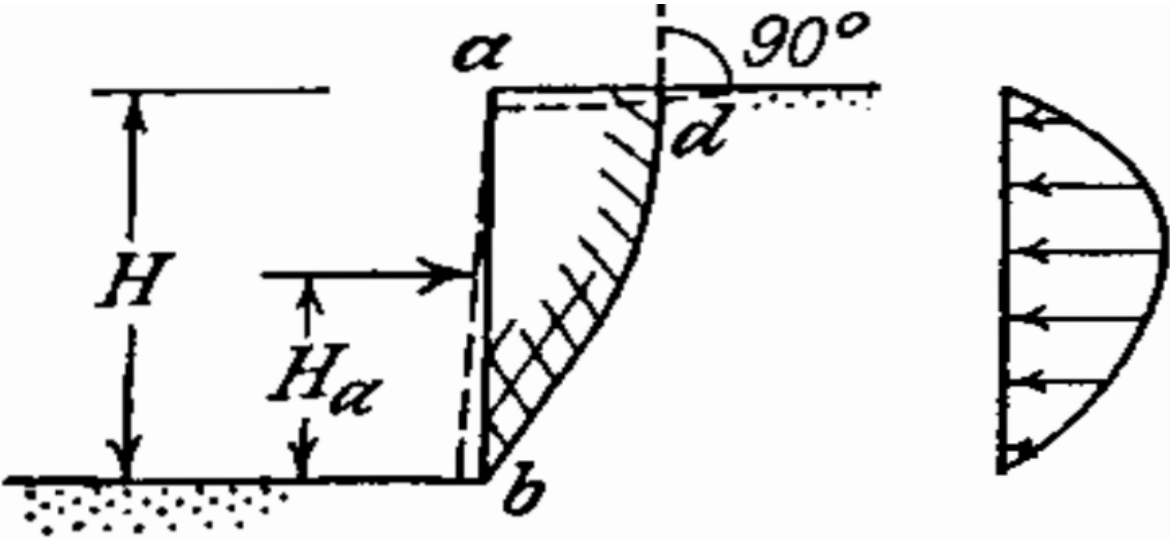
This investigation examines the behavior of inverted T-shaped cantilever retaining wall through 3D numerical analyses, where the real shape and thickness of the structure are explicitly modeled and the structural elements are simulated as continuum.

## 2.7. Effect of Soil Arching on Lateral Soil Pressures

Terzaghi (1943) proposed that, if one part of support of a mass of soil yield while the remainder stays in place the soil adjoining the yielding part moves out of its original position between adjacent stationary mass of soil. The relative movement within the soil is opposed by a shearing resistance with in the zone of contact between the yielding and the stationary masses. Since the shearing resistance tends to keep the yielding mass in its original position, it reduces the pressure on the yielding part of the support and increase the pressure on the adjoining stationary part. This transfer of pressure from a yielding mass of soil onto the adjoining stationary parts is commonly called the *arching effect* and the soil is said to *arch* over the yielding part of the support. Arching also takes place if one part of a yielding support moves out more than the adjoining parts.

Arching effect is encountered in many geotechnical problems such as conduits covered with an embankment, backfilled trenches overlying conduits and backfills behind retaining walls. Studies related to soil arching starts with the classical arching theories of Terzaghi (as cited on Ertuğrul, 2013). Terzaghi (1943) investigated, arching in the sand adjoining a vertical support whose lower part yields in an outward direction. In figure 2.7, the lateral support is represented by *ab* the surface of the sand is horizontal and the support yields by tilting around its upper edge. After the support has yielded sufficiently, a shear failure occurs in the sand along a surface of sliding *bd* which extends from the foot *b* of the support to the surface of the sand. The stationary position of the upper edge, *a*, of the lateral support prevents a lateral expansion of the upper part of the sliding wedge. Therefore, the sand grains located in the upper part of the wedge can move only in a downward direction. Hence the surface of sliding intersects the horizontal surface of the sand at *d* at right angles. The corresponding subsidence of the surface of the sliding wedge is indicated in figure by a dashed line.

The lateral expansion of the lower part of the sliding wedge is associated with a shortening in a vertical direction. The corresponding subsidence of the upper part of the wedge is opposed by the frictional resistance along the adjoining steep part of the surface of sliding. As the consequence the vertical pressure on the lower part of the wedge is smaller than the weight of the sand located above it. This phenomenon constitutes the arching effect in the sand behind yielding lateral supports whose upper part is stationary.



**Figure 2.7** Shear failure in sand due to yield of lateral support by tilting about its upper edge.

## **CHAPTER 3**

### **3. FINITE ELEMENT MODELING**

#### **3.1. Numerical Modelling Software**

In this study the geometry of the finite element model was constructed using the graphical input procedure of the PLAXIS 3D connect edition V20 which is a special purpose three-dimensional finite element program (PLAXIS 3D, Reference manual) used to perform deformation, stability and flow analysis for various types of geotechnical applications such as excavation, foundations, embankments and tunnels. Geotechnical projects require advanced constitutive models for the simulation of the nonlinear, time dependent and anisotropic behavior of soil and rock. PLAXIS can be used to model different element types, such as different types of retaining walls, various types of loads behind the wall and the interface elements between the retaining walls and the soil.

#### **3.2. PLAXIS Model Setup**

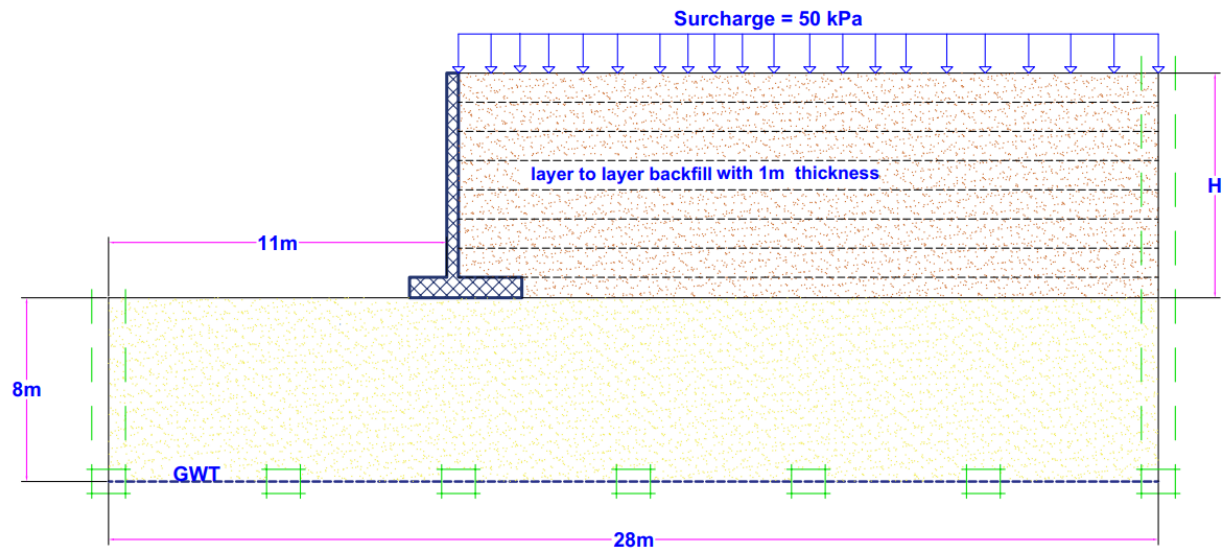
To carry out the finite element analysis using PLAXIS 3D program the modelling process completed in five modes namely soil, structure, mesh, flow condition and staged construction. The soil stratigraphy, the general water level and the initial condition of soil layers are defined in soil mode. The geometric entities as well as the structural elements and forces in the project are defined in structure mode. The geometry models created in structure mode were discretized and the finite element mesh is generated in the mesh mode.

##### **3.2.1. Initial and Boundary Conditions**

For all the models used in this study, standard fixities were applied. In PLAXIS 3D standard boundary conditions, vertical model boundaries with their normal in x-direction (i.e., parallel to yz-plane) are fixed in x-direction and free in y-and z-direction. Vertical model boundaries with



their normal in y-direction (i.e., parallel to xz-plane) are fixed in y-direction and free in x-and z-direction. The model bottom boundary is fixed in all directions and the top surface is free in all directions (Figure 3.1). The ground water level is found at the bottom surface of the foundation soil, for that matter the water load on the retaining structure is neglected.



**Figure 3.1.** Model which shows fixities applied for boundary conditions, soil layer thickness, ground water level and initial conditions.

Following the setting of finite element computation parameters, the PLAXIS input program (PLAXIS 3D, Reference manual) is used for the generation of model's finite element mesh. The loading input "staged construction" is used, it allows to define the different construction steps. Staged construction is the loading type which enables the user to specify a new state that is to be reached at the end of calculation phases. Since it is performed with the load advancement ultimate level procedure, it is controlled by a total multiplier (PLAXIS 3D, Reference manual section 7.4.1). As default in PLAXIS the first phase is an in-situ stress calculation. It is the starting point of the forthcoming construction of the super structure. The in-situ value is calculated by  $K_0$ -procedure or gravity loading.  $K_0$ -procedure is a spatial calculation method available in PLAXIS to define the initial stresses for the model, taking in to account the loading history of the soil. The parameters required in the initial stress's development procedures are defined in the initial tab sheet of material data sets for soil and interfaces. In practice, the value of  $K_0$  for normally consolidated soil is often assumed to be related to the friction angle by Jaky's empirical expression;

$$K_0 = 1 - \sin\phi \quad (3.1)$$

In PLAXIS 3D, Reference manual (section 6.17) for an over-consolidated soil,  $K_0$  would be expected to be larger than the value given by the expression. For Mohr-Coulomb model, the default value of  $K_0$ -value is based on Jaky's formula. For the advanced models the default value is based on the  $k_0^{nc}$  parameter and also influenced by the over consolidation ratio (OCR) or the pre-overburden pressure (POP).

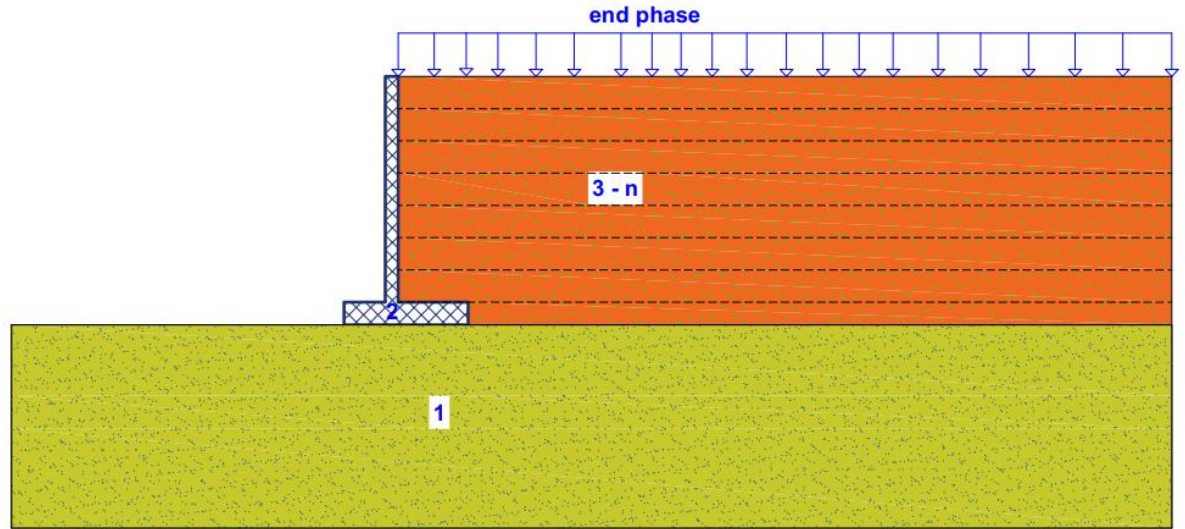
For Hardening soil model;

$$K_0 = k_0^{nc} OCR - \frac{v_{ur}}{1-v_{ur}} (OCR - 1) \quad (3.2)$$

Petersson (2012), depicted that, the  $K_0$ -procedure particularly suitable in case with horizontal surface and all soil layers and phreatic level parallel to the surface. For gravity loading the in-situ situation is decided by volumetric weight. It is preferred in situations with sloping ground or non-horizontal layering of soil. When  $K_0$ -procedure is adopted, PLAXIS will generate vertical stresses that are in equilibrium with the self-weight of the soil.

After the in-situ calculation, the model could be divided into different phases that represented how it was constructed in reality. The calculation phase was preceded by the initial condition stage, simulating the disturbances induced to the soil foundation by the wall weight before the beginning of the backfilling process. As the wall placed (disturbance of sand foundation with wall weight), continues stage by stage backfill with 1m thickness for each layer was executed with in the calculation and finally the surcharge load is applied. A step by step staged simulation presented as;

- Initial phase or in-situ calculation (1).
- Construction of cantilever wall by activating wall geometry and interface (2).
- Construction of backfill divided into layers with 1 m thickness, (3 - n). where n – represents the number of backfill layers which depends on the wall height.
- Application of surcharge load (end phase).



**Figure 3.2.** Phases in PLAXIS model.

### 3.3. Material Constitutive Model and Parameters

#### 3.3.1 Soil Modelling

In the present numerical analysis, the soil has been modeled using hardening soil model, incorporated in to PLAXIS program, considered in drained soil condition, which means no excess pore pressures are generated. Since, the ground water table is found below the bottom of foundation soil, this drainage type is usually used for dry soil and also for full drainage due to high permeability(sand).

The hardening soil model is an advanced model for simulating the behavior of different types of soil, both soft soils and stiff soils, Schanz (as cited in PLAXIS 3D Material mode). In contrast to an elastic perfectly-plastic model, the yield surface of Hardening soil model is not fixed in principal stress space, but it can expand due to plastic straining. Distinction is made between two main types of hardening, namely shear hardening and compression hardening. Shear hardening is used to model irreversible strains due to primary deviatoric loading. Compression hardening is used to model irreversible plastic strains due to primary compression in oedometer loading and isotropic loading. Both types of hardening are contained in the present model.

A basic idea for the formulation of the Hardening-soil model is the hyperbolic relationship between the vertical strain  $\varepsilon_1$ , and the deviatoric stress,  $q$ , in primary tri-axial loading. When subjected to primary deviatoric loading, soil shows a decrease stiffness and simultaneously irreversible plastic strains developed. Kondner & Zelasko (as cited in T.Schanz , P.A. Vermeer & P.G. Bonnier,1999) depicted that, in the special case of drained tri-axial test, the observed relationship between the axial strain and the deviatoric stress can be well approximated by a hyperbola. Standard drained tri-axial tests tend to yield curves that can be described by:

$$\varepsilon_1 = \frac{q_a}{E_{50}} \frac{(\sigma_1 - \sigma_3)}{q_a - (\sigma_1 - \sigma_3)} \quad \text{for } q < q_f. \quad (3.3)$$

The ultimate deviatoric stress,  $q_f$  and the asymptotic value,  $q_a$  are defined as:

$$q_f = \frac{6 \sin \varphi_p}{3 - \sin \varphi_p} (p + c \cot \varphi_p) \quad q_a = \frac{q_f}{R_f} \quad (3.4)$$

The above relationship for  $q_f$  is derived from the Mohr-Coulomb failure criterion, which involves the strength parameters  $c$  and  $\varphi_p$ . As soon as  $q = q_f$ , the failure criterion is satisfied and perfectly plastic yielding occurs. The ratio between  $q_f$  and  $q_a$  is given by failure ratio  $R_f$  which should obviously be smaller than 1.  $R_f = 0.9$  often is a suitable default setting. This hyperbolic relationship is plotted in Figure 3.3.

### 3.3.1.1 Stiffness for Primary Loading

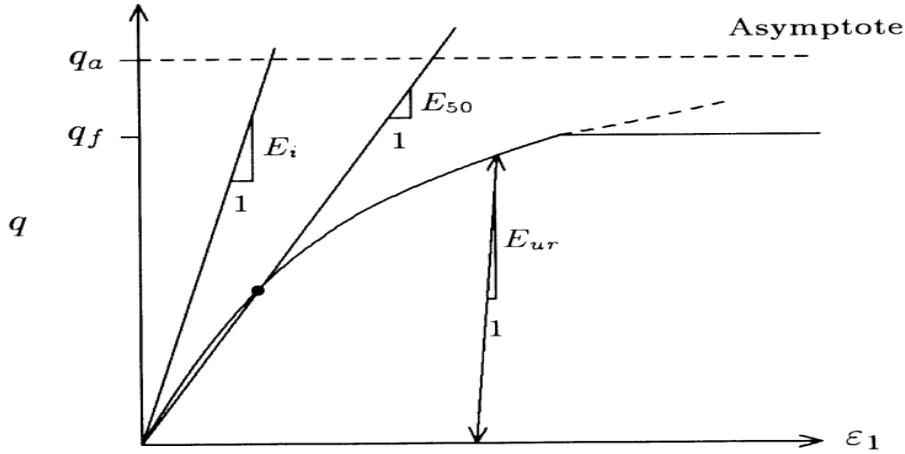
The stress strain behavior for primary loading is highly nonlinear. The parameter  $E_{50}$  is the confining stress dependent stiffness modulus for primary loading.  $E_{50}$  is used instead of the initial modulus  $E_i$  for small strain which, as a tangent modulus, is more difficult to determine experimentally. It is given by the equation:

$$E_{50} = E_{50}^{ref} \left( \frac{\sigma_3 + c \cot \varphi_p}{\sigma^{ref} + c \cot \varphi_p} \right)^m \quad (3.5)$$

$E_i$  is related to  $E_{50}$  by:

$$E_i = \frac{2E_{50}}{2 - R_f} \quad (3.6)$$

$E_{50}^{ref}$  is a reference stiffness modulus corresponding to the reference stress  $p^{ref}$ . The actual stiffness depends on the minor principal stress,  $\sigma_3'$ , which is effective confining pressure in a tri-axial test. The amount of stress dependency is given by the power  $m$ .



**Figure 3.3.** Hyperbolic stress-strain relation in primary loading for a standard drained tri-axial test (Schanz, Vermeer and Bonnier, 1999).

### 3.3.1.2. Stiffness for Un-/Reloading

For unloading and reloading stress paths, another stress-dependent stiffness modulus is used:

$$E_{ur} = E_{ur}^{ref} \left( \frac{\sigma_3 + c \cot \phi_p}{\sigma^{ref} + c \cot \phi_p} \right)^m \quad (3.7)$$

Where  $E_{ur}^{ref}$  is the reference young's modulus for unloading and reloading, corresponding to the reference pressure  $\sigma^{ref}$ . Doing so the un-/reloading path is modeled as purely(non-linear) elastic. The elastic shear modulus using a constant value for un-/reloading poison's ratio  $\nu_{ur}$ .

$$G_{ur} = \frac{1}{2(1+\nu_{ur})} E_{ur}, \quad \sigma^{ref} = 100kPa. \quad (3.8)$$

### 3.3.1.3. Oedometer Stiffness

The triaxial modulus largely controls the shear yield surface and the oedometer modulus controls the cap yield surface. In fact,  $E_{50}^{ref}$  largely controls the magnitude of the plastic strain that are associated with the shear yield surface. Similarly,  $E_{oed}^{ref}$  is used to control the magnitude of plastic strains that originate from the yield cap (Schanz, Vermeer and Bonnier, 1999).

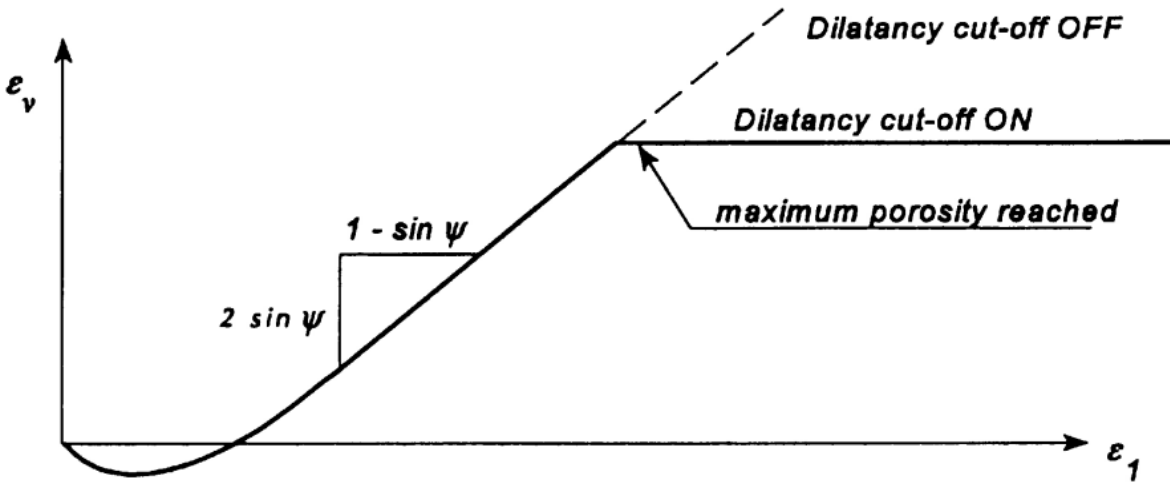
In contrast to elasticity-based models, the elastoplastic Hardening-soil model does not involve a fixed relationship between the drained tri-axial stiffness  $E_{50}$  and the oedometer stiffness  $E_{oed}$ . Instead, this stiffness must be given independently. To define the oedometer stiffness we use

$$E_{oed} = E_{oed}^{ref} \left( \frac{\sigma_3 + c \cot \phi_p}{\sigma^{ref} + c \cot \phi_p} \right)^m \quad (3.9)$$

Where  $E_{oed}$  is a tangent stiffness modulus for primary loading, Hence,  $E_{oed}^{ref}$  is a tangent stiffness at vertical stress of  $\sigma_1 = \sigma^{ref}$ .

### 3.3.1.4. Dilatancy Cut-Off

After the extensive, dilating material arrive in a state critical density where dilatancy has come to end. This phenomenon of soil behavior is included in the hardening soil model by means of dilatancy cut-off. In order to specify this behavior, the initial void ratio,  $e_0$ , and maximum void ratio,  $e_{cv}$ , of material are entered in PLAXIS 3D program. As soon as the volume change results in a state of maximum void, the mobilized dilatancy angle,  $\psi_m$ , is automatically set back to zero, as indicated in Equation 3.9 and Figure 3.4:



**Figure 3.4** Resulting strain curve for a standard drained triaxial test including dilatancy cut-off (Schanz, Vermeer and Bonnier, 1999).

$$\begin{aligned} \text{For } e < e_{cv}, \quad \sin \psi_m &= \frac{\sin \psi_m - \sin \psi_{cv}}{1 - \sin \psi_m \sin \psi_{cv}}, \\ \text{For } e \geq e_{cv}, \quad \sin \psi_m &= 0 \end{aligned} \quad (3.10)$$

### 3.3.1.5. Parameters of The Hardening-Soil Model

Some parameters of the Hardening model coincide with those of the Mohr-Coulomb model. These are the failure parameters  $\varphi_p$ ,  $c$  and  $\psi_p$ . Additionally, we use the basic parameters for the stiffness:

$E_{50}^{ref}$ , secant stiffness in standard drained tri-axial test,

$E_{oed}^{ref}$ , tangent stiffness for primary oedometer loading and

$m$ , power for stress-level dependency of stiffness.

This set of parameters is completed by the following advanced parameters:

$E_{ur}^{ref}$ , unloading/reloading stiffness,

$\nu_{ur}$ , poisson's ratio for unloading-reloading,

$p^{ref}$ , reference stress for stiffness,

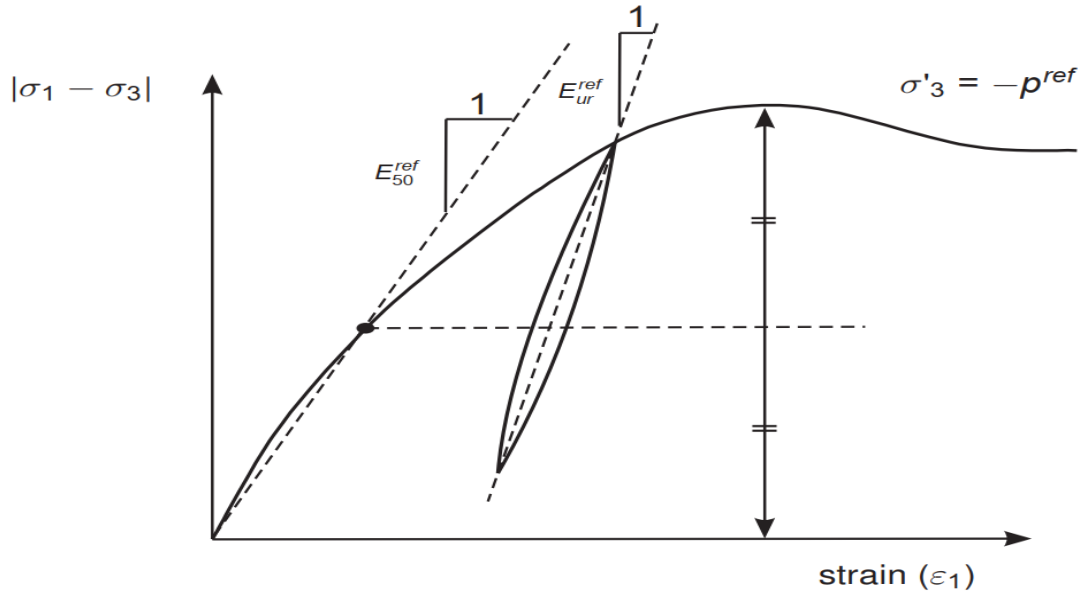
$K_0^{NC}$ ,  $K_0$ -value for normal consolidation and

$R_f$ , failure ratio  $q_f/q_a$ .

### 3.3.1.5.1. Stiffness moduli, $E_{50}^{ref}$ , $E_{oed}^{ref}$ and $E_{ur}^{ref}$ and power m

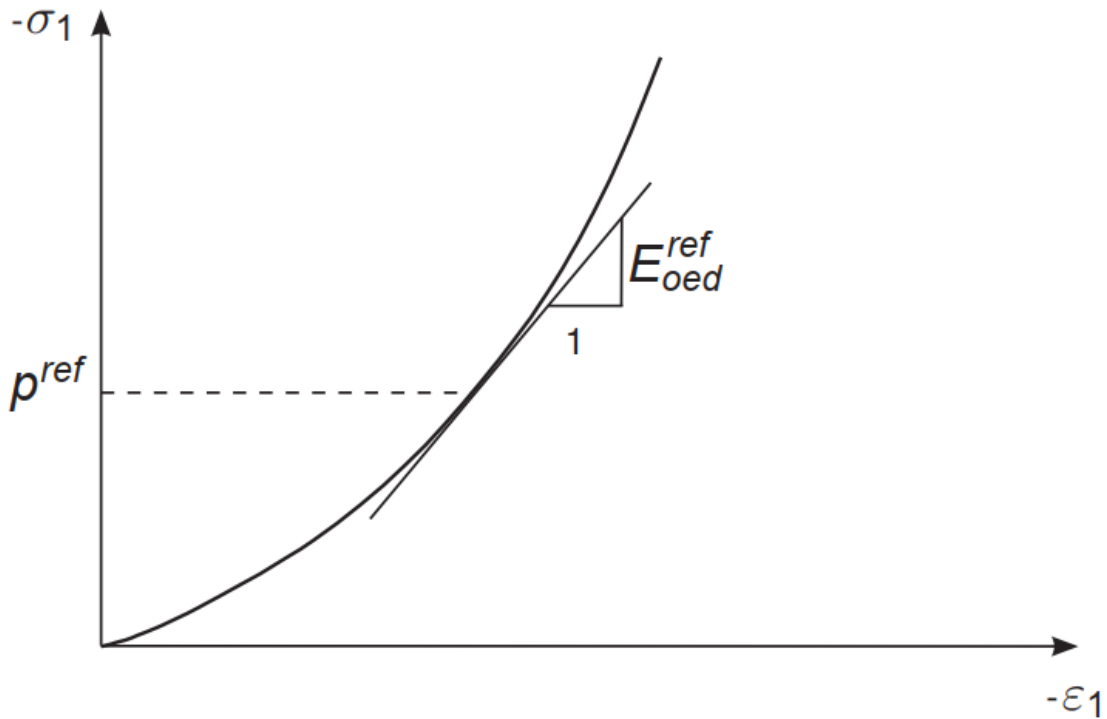
The advantage of the Hardening soil model over the Mohr-Coulomb model is not only the use of hyperbolic stress-strain curve instead of a bi-linear curve, but also the control of stress level dependency. When using the perfectly plastic Mohr-Coulomb model, the user has to select a fixed value of young's modulus whereas for real soils this stiffness depends on the stress level. It is therefore necessary to estimate the stress levels within the soil and use these to obtain suitable values of stiffness. Instead, a stiffness modulus  $E_{50}^{ref}$  is defined for a reference minor principal effective stress of  $-\sigma'_3 = p^{ref}$ . This is the secant stiffness at 50% of maximum deviatoric stress, at the cell pressure equal to the reference stress  $p^{ref}$  (Figure 3.5). As the default value, the program uses  $p^{ref} = 100\text{kN/m}^2$ .





**Figure 3.5.** Definition of  $E_{50}^{ref}$  and  $E_{ur}^{ref}$  for drained tri-axial test results (Schanz, Vermeer and Bonnier, 1999).

As indicated in Figure 3.9  $E_{oed}$  is a tangent stiffness modulus obtained from the oedometer test, Hence,  $E_{oed}^{ref}$  is a tangent stiffness at a vertical stress  $-\sigma'_1 = \frac{-\sigma'_3}{K_0^{nc}} = p^{ref}$ . Not that we basically use  $\sigma'_1$  rather than  $\sigma'_3$  and that we consider primary loading.



**Figure 3.6.** Definition of  $E_{oed}^{ref}$  in oedometer test result (Schanz, Vermeer and Bonnier, 1999).

In many practical cases it is appropriate to set  $E_{ur}^{ref}$  is equal to  $3E_{50}^{ref}$ , and  $E_{50}^{ref} = E_{oed}^{ref}$ ; is the default setting used in PLAXIS. Lengkeek (2003) addressed that, for cohesion less material such as sand the value of secant stiffness in standard drained tri-axial test  $E_{50}^{ref}$  estimated from cone resistance. Research on sand has shown that the cone resistance is controlled by the relative density ( $D_r$ ), in situ stresses and compressibility. Kulhawy et al. 1990 (as cited in H.J. Lengkeek, 2003) suggested a formula for estimating the relative density which can be rewritten to the formula:

$$D_r \propto qc^{0.5} \sigma_v'^{-0.25}$$

The  $E_{50}^{ref}$  is directly proportional to relative density ( $D_r$ ),

$$E_{50}^{ref} = 60 * D_r \tag{3.11}$$

Where:

$D_r$ =relative density.

$E_{50}^{ref}$  = HS-model references tri-axial loading stiffness (MPa)

60 = constant (MPa)

Aye, Phien-wej & Humza (2012) performed a numerical study incorporating the Hardening Soil model to examine its applicability in capturing the diaphragm wall, and they recommend value of power for stress-level dependency of stiffness  $m$ , taken 0.8 for sand from loose to dense and 0.5 for very dense sand, and they correlate Hardening soil parameter with Number of blows as  $E_{50}^{ref}$  (kN/m<sup>2</sup>) for sand loose to medium dense 750N and for sand dense to very dense 1000N. The value of modeling stiffness parameter used in this analysis estimated from the relation between stiffness parameter and relative density was taken to achieve better value.

### 3.3.2 Modelling of Interface Element

Interface elements between the wall and the backfill were taken into account in the analyses. Interfaces are joint elements (PLAXIS, Reference manual) to be added in to plates to allow for proper modelling of soil structure interaction. For soil structure interaction, 12-node interface elements are used to simulate the behavior. Each interface has assigned to it a virtual thickness which is an imaginary dimension used to define the material properties of the interface. The interface element had zero thickness in the finite element formulation. However, an interface element is supposed to generate very little elastic deformation and therefore the virtual thickness should be small. The virtual thickness is calculated as the virtual thickness factor (0.1 which is default value) times the global element size. The material properties of the interface element were the same as those of surrounding soil elements, except the strength reduction factor ( $R_{int}$ ), defined as the ratio of the interface strength to the shear strength of the surrounding soils, was used for the interface element. In order to fix the value of the strength/stiffness reduction factor I had search literatures on the interaction between soil and concrete structures but detailed information not found. In the absence of detailed information, PLAXIS reference manual recommends that, it may have assumed that  $R_{int}$  is the order of 2/3. For this investigation the interaction of soil to concrete structure, the value of strength/stiffness reduction factor,  $R_{int} = 0.67$  was used. The interfaces in PLAXIS are generally modeled using zero-thickness elements. These interfaces have properties of

friction angle ( $\phi_i$ ), cohesion ( $c_i$ ), dilatancy angle ( $\psi_i$ ), shear modulus ( $G_i$ ), Poisson's ratio, and oedometer modulus ( $E_{oed, i}$ ). The values of interface properties in PLAXIS can be set directly by using a strength/stiffness reduction factor ( $R_{int}=0.67$ ). The value  $R_{int} = 0.67$  represents a structure and soil bonded with interface strength reduced by this value. This factor is applied to the properties of the adjacent soil as follows:

$$c_i = R_{int} c_{soil} \quad (3.12)$$

$$\phi_i = \tan^{-1} (R_{int} \tan \phi_{soil}) \quad (3.13)$$

$$\psi_i = \begin{cases} 0 & R_{int} < 1 \\ \psi_{soil} & R_{int} = 1 \end{cases} \quad (3.14)$$

$$G_i = R_{int}^2 G_{soil} \quad (3.15)$$

$$E_{oed, i} = 2G_i \frac{1-\nu_i}{1-2\nu_i} \quad (3.16)$$

where:  $c_{soil}$  is the soil cohesion;  $\phi_{soil}$  is the soil friction angle;  $\psi_{soil}$  is the soil dilatancy angle, and;  $G_i$  is the soil shear modulus. The interface strength factor can be set using the following options:

**Rigid:** The option is used when the interface should not have a reduced strength with respect to the strength in the surrounding soil. The strength of these interfaces should be assigned as Rigid corresponds to  $R_{int} = 1.0$ .

**Manual:** The value of  $R_{int}$  can be entered manually if the interface strength is set to manual.

In the numerical analysis of this study the backfill material of dense sand and cohesive foundation soil were considered. The values of soil model parameters used in this analysis are presented in Table 3.1.

**Table 3.1:** Material properties for Backfill and Foundation soil.

Parameter	Name	Unit	Backfill soil	Interface	Foundation soil
-----------	------	------	---------------	-----------	-----------------

Material model	Model	–	Hardening soil model	Hardening soil model	Hardening soil model
Drainage Type	Type	–	Drained	Drained	Drained
Unit weight above the phreatic level	$\gamma_{\text{unsat}}$	kN/m <sup>3</sup>	16.5	16.5	16
Unit weight below the phreatic level	$\gamma_{\text{sat}}$	kN/m <sup>3</sup>	20	20	19
Reference secant stiffness for triaxle test	$E_{50}^{\text{ref}}$	kN/m <sup>2</sup>	13000	13000	34000
Tangent oedometer stiffness	$E_{\text{oed}}^{\text{ref}}$	kN/m <sup>2</sup>	13000	13000	34000
Unloading/reloading stiffness	$E_{\text{ur}}^{\text{ref}}$	kN/m <sup>2</sup>	39000	39000	102000
Power for stress level	m	–	0.5	0.5	1
Cohesion	$c_{\text{ref}}$	kN/m <sup>2</sup>	0	0	10
Friction angle	$\phi$	°	39	39	30
Dilatancy angle	$\psi$	°	9	9	0
Poisson's ratio	$\nu_{\text{ur}}^{(\text{nu})}$	–	0.3	0.3	0.3
Interface strength	–	–	Manual	Rigid	Manual
Interface reduction factor	$R_{\text{inter}}$	–	0.67	1	0.67
$K_0$ determination	–	–	Automatic	Automatic	Automatic
Lateral earth pressure coefficient	$K_0$	–	0.3707	0.3707	0.5000
Over-consolidation ratio	$OCR$	–	1.000	1.000	1.000
Pre-overburden pressure	$POP$	–	0.000	0.000	0.000

*Automatic* allows the PLAXIS program to take equation 3.2 for  $K_0$  determination.

### 3.3.3. Wall Modelling

The retaining wall structure was modeled using linear elastic model and the geometry of wall created as a plate element. The stiffness of wall represented young's modulus of reinforced

concrete  $E$ , which is depends on the concrete class. In this investigation the wall to be simulated in the numerical analysis graded as C-25 reinforced wall. The equation of  $E$  taken from EBCS code of standard.

$$E = 9.5(f_{ck}+8)^{1/3} \quad (3.17)$$

$f_{ck}$  = Concrete grade/ conversion factor (1.25 constant)

$$= 25/1.25$$

$$= \underline{20(\text{MPa})}$$

$$\text{So, } E = 9.5(20+8)^{1/3}$$

$$= \underline{29\text{GPa}}$$

Where,  $E$  = The elasticity(young's) modules in GPa,

$f_{ck}$  = characteristic cylinder comprehensive strength which is depend on grade of concrete in MPa.

The wall modelling parameters are presented in Table below.

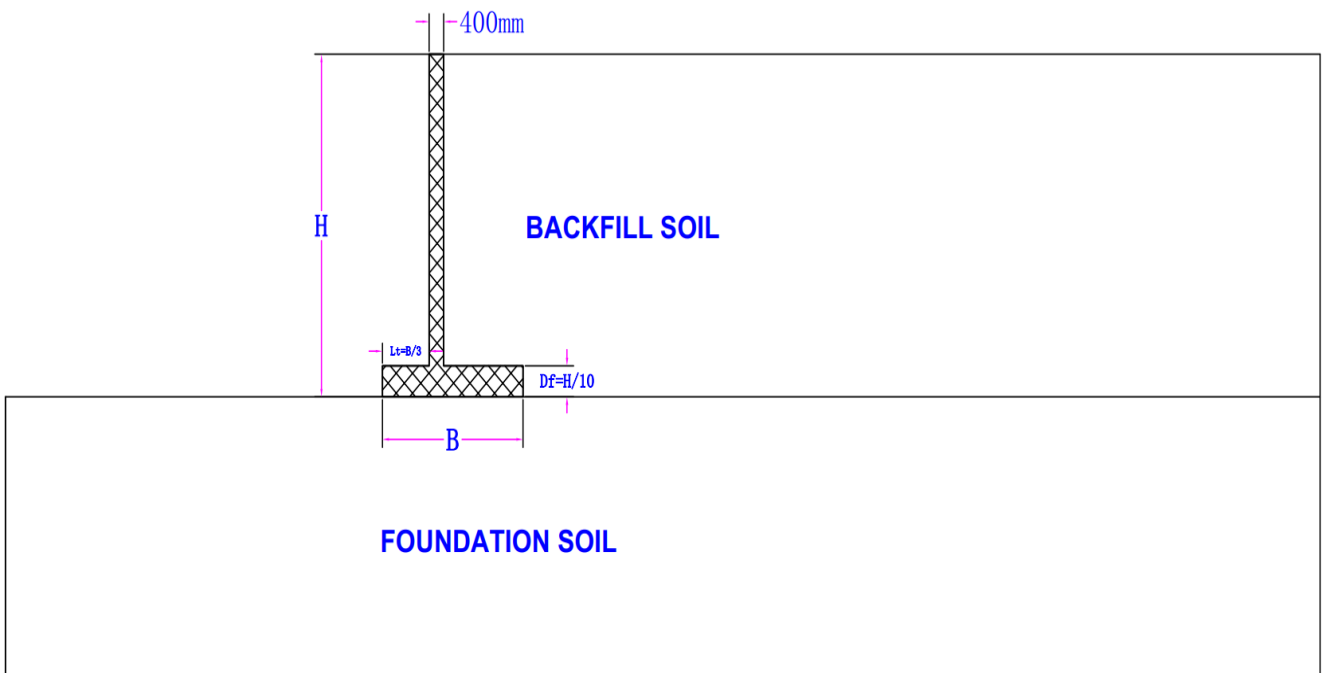
**Table 3.2:** Wall modelling parameters.

Parameter	Name	Unit	Wall
Material type	Type	–	Reinforced concrete
Material model	Model	–	Linear elastic
Unit weight	$\gamma$	kN/m <sup>3</sup>	24
Young's modulus	$E$	kPa	29x10 <sup>6</sup>
Poisson's ratio	$\nu$	–	0.2

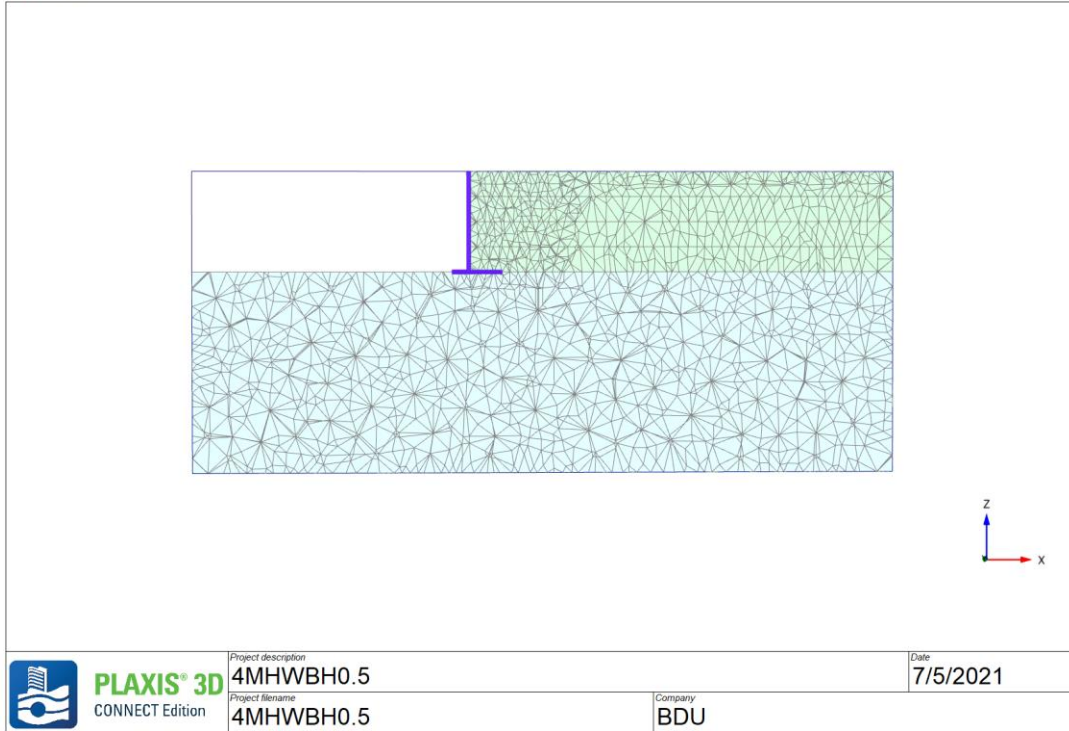
### 3.3.4. Geometry of Wall

In order to investigate the effect of the dimension of wall i.e., the height of wall ( $H$ ) with proportioned base width ( $B$ ), Three inverted T type cantilever retaining walls were considered, 4m height wall designated by(4MHW), 6m height wall (6MHW), and 9m height wall (9MHW) and the schematic sample wall dimensions were presented in Figure 3.7, 3.8 and 3.9. To provide resistance

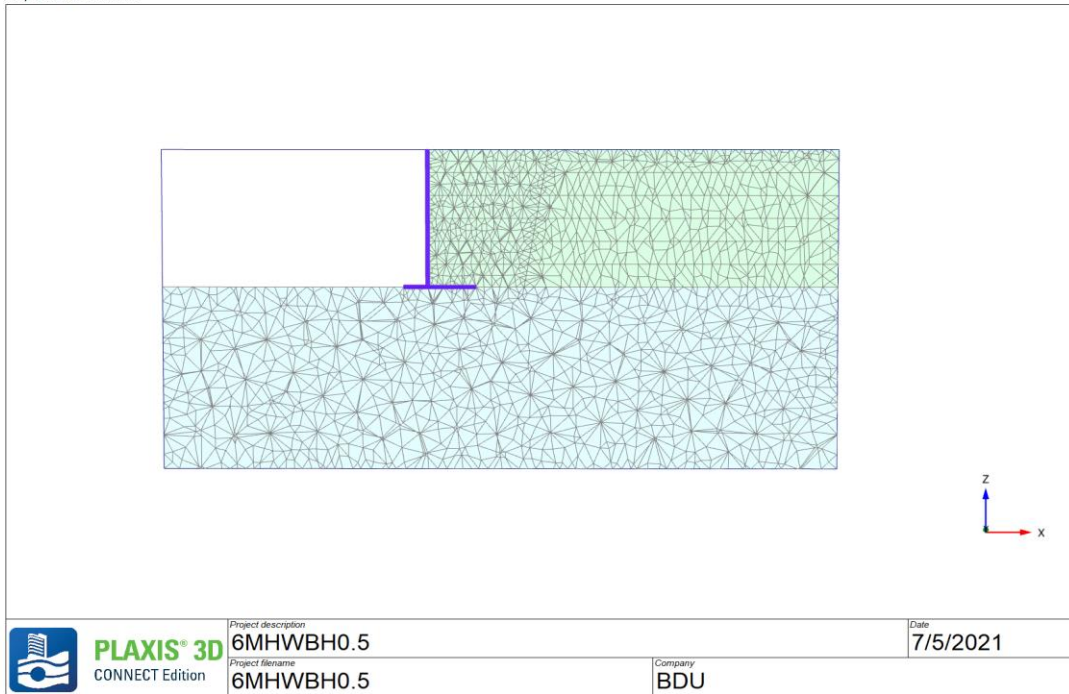
to overturning and sliding, the design of cantilever retaining wall starts by proportioning the wall dimension. Ranjan and Rao, 2007 (as cited on Dahunsi, Adewuyi and Adedokun, 2015) recommended the following values for the stability of cantilever retaining walls, minimum top width of stem 200 mm, Base width,  $B = 0.4H$  to  $0.7H$  and projection of toe from the base of the stem to be  $0.2B$  to  $0.4B$ . Considering this criteria, for this numerical investigation the dimension of wall taken as top width of stem to be 400mm, the ratio of base width  $B$  to stem height  $H$  ranging from 0.4 to 0.7, projection of toe from the stem base ( $L_t$ ) =  $B/3$  and thickness of base width ( $D_f$ ) =  $H/10$ .



**Figure 3.7.** Typical geometry of walls.

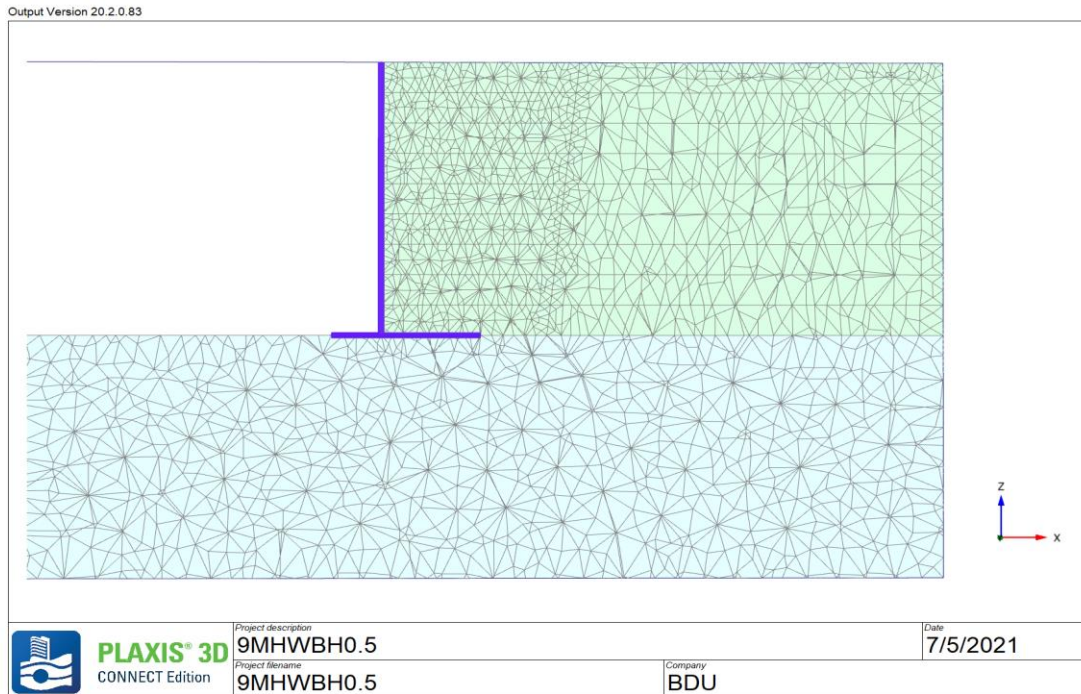


**Figure 3.8.** Four-meter height wall (4MHW) section view.



**Figure 3.9.** Six-meter height wall (6MHW) section view.





**Figure 3.10.** Nine-meter height wall (9MHW) section view.

The present approach allowed to investigate the direct effect of the parameters  $H$  and  $B/H$  on the displacement pattern and the lateral pressure acting on the T-shaped retaining wall. The values of  $H$  considered were assumed to represent the behavior of distinctive wall dimensions including the height of the wall considered in the development of the numerical model ( $H=9$  m). The combination of the ( $H$ ) and ( $B/H$ ) parameters yield to the numerical analysis of 12 different T-shaped retaining walls. The designation adopted for the different parametric walls is presented in the Table 3.3, were for example the wall designated by 4MHWB/H0.4 stands for a 4-meter height T-shaped wall with a ratio of base width over height ( $B/H$ ) equal to 0.4 ( $B/H0.4$ )

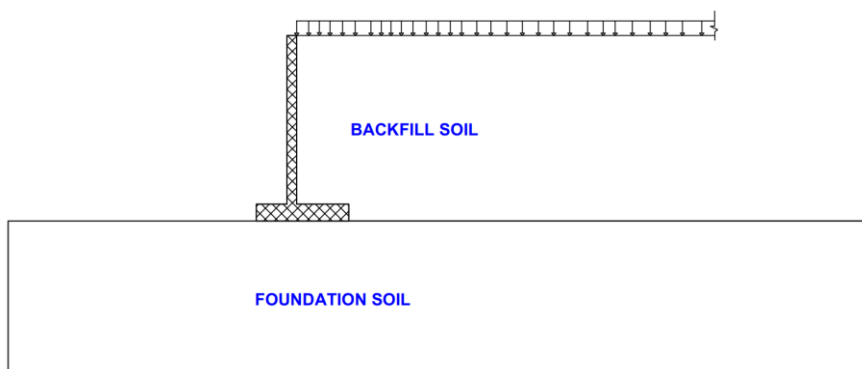
**Table 3.3:** Designation of wall dimension with backfill sand.

<b>H(m)</b>	<b>B/H</b>			
	<b>0.4</b>	<b>0.5</b>	<b>0.6</b>	<b>0.7</b>
4	4MHWB/H0.4	4MHWB/H0.5	4MHWB/H0.6	4MHWB/H0.7
6	6MHWB/H0.4	6MHWB/H0.5	6MHWB/H0.6	6MHWB/H0.7

9	9MHWB/H0.4	9MHWB/H0.5	9MHWB/H0.6	9MHWB/H0.7
---	------------	------------	------------	------------

### 3.2.3.6. Surcharge Load Distribution Method

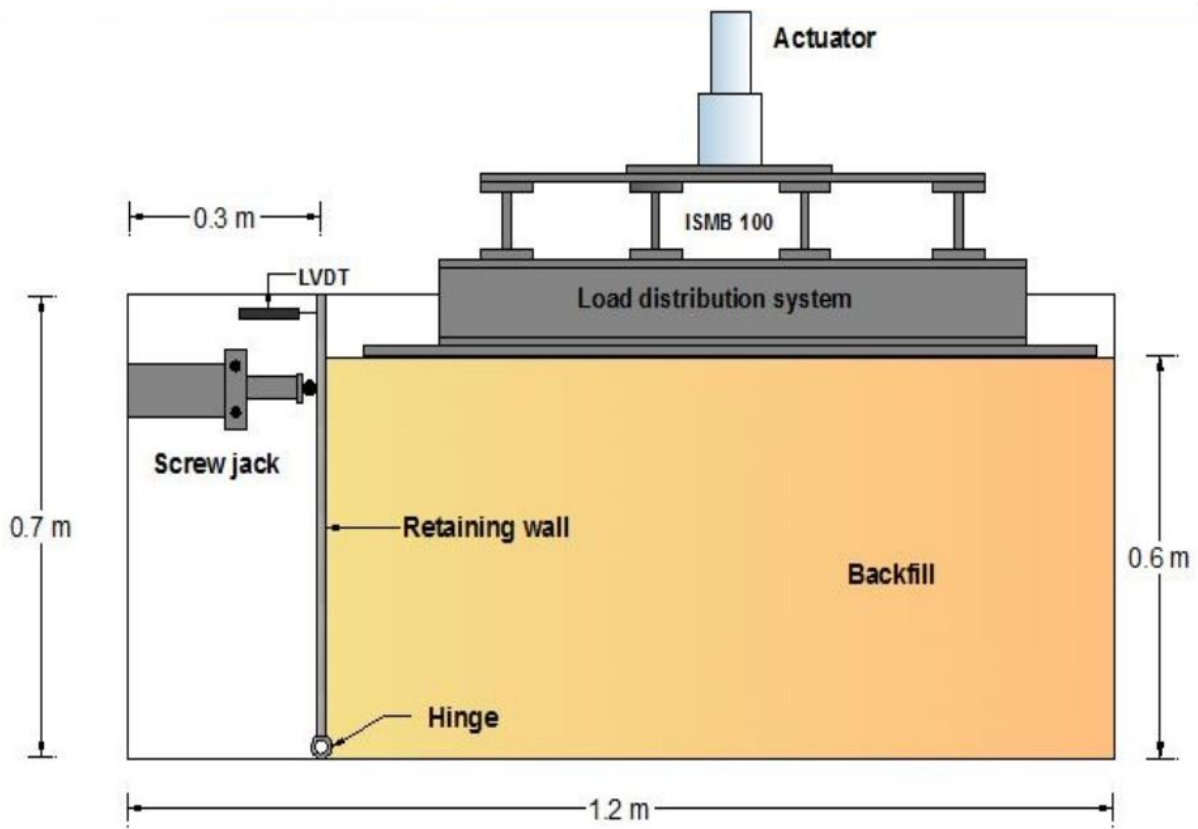
The simplest way to model the surcharge load on top of the soil next to the cantilever wall is by simply assuming that it extends indefinitely as shown in Figure 3.11. This will give an increase in stress in the entire soil mass by 50 kPa.



**Figure 3.11.** Illustration of surcharge load.

## 3.4. Validation

Experimental study on the lateral earth pressure distribution on retaining wall (Rizwan Khan et al. 2016) was used for validation. To study the distribution of lateral pressure on retaining wall, 1-g small scale physical model tests were carried out using a stainless-steel tank having dimension of 1.2 m length, 0.31 m width and 0.7 m depth. A mechanical jack is fixed at the non-backfilled side of the tank to hold the wall in position to ensure at-rest conditions. Figure 3.12, shows details of the experimental setup. To apply uniformly distributed static loading on the surface of backfill, load distribution system, was placed in such a way that load can be distributed uniformly at the backfill. Static surcharge of 10-50 kPa was applied with an increment of 10 kPa using a hydraulic actuator.



**Figure 3.12.** Detailed diagram of experimental setup of physical model test used for validation (Rizwan Khan et al. 2016).

The lateral earth pressure distribution determined with FE analyses of 0.6m height retaining wall and it was compared with the results of experimental study. The lateral earth pressure ( $\sigma_{horizontal}$ ) and normalized depth( $z/H$ ) are used for verifications.

### 3.4.1. Hardening Soil Model Parameter Determination

The input parameters for Mohr-Coulomb material model were gained from the literature (Rizwan Khan et al. 2016). The studies from which these properties were obtained consisted of foundation soil and backfill soil properties used for Mohr-Coulomb material model as shown in table 3.4.

**Table 3.4:** Input parameters of soil and wall for validation (data from Rizwan Khan et al. 2016).

Parameters	Name	Unit	Foundation soil	Backfill soil	Wall
Unit weight	$\gamma$	kN/m <sup>3</sup>	16	16.5	25
Young's modulus,	E	MPa	34	13	29e6
Cohesion	c	kN/m <sup>2</sup>	10	0	–
Friction angle	$\phi$	°	30	39	–
Dilatancy angle	$\psi$	°	0	9	–
Poisson's ratio	$\nu$	–	0.33	0.3	0.2

The hardening soil model, while giving a better representation of soil material behavior, requires a number of specific parameters to do so, these parameters have not been described in experimental study.

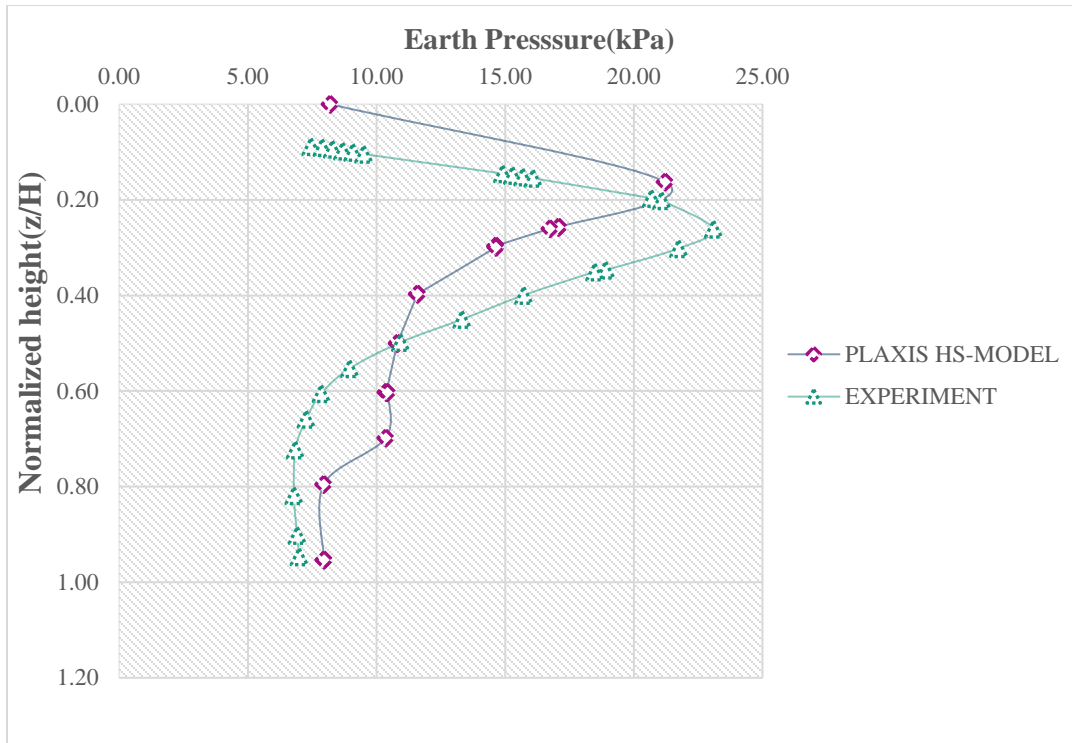
In order to define the input parameters for Hardening Soil model, no information was known to compare and calibrate, so some correlations recommended by PLAXIS were utilized. First, the  $E_{50}^{ref}$  given by PLAXIS for the known Young's Modulus and Mohr Coulomb Criterion was used. Second,  $E_{50}^{ref} = E_{oed}^{ref}$  and the  $E_{ur}^{ref}$  was taken as  $3E_{50}^{ref}$  as recommended for use in PLAXIS. Then the recommended m value was adjusted from different studies to fit most approximately the experimental data with the Hardening Soil model.

**Table 3.5:** Material properties for backfill and foundation soil.

Parameter	Name	Unit	Backfill soil	Interface	Foundation soil
Material model	Model	–	Hardening soil model	Hardening soil model	Hardening soil model
Drainage Type	Type	–	Drained	Drained	Drained
Unit weight above the phreatic level	$\gamma_{unsat}$	kN/m <sup>3</sup>	16.5	16.5	16
Unit weight below the phreatic level	$\gamma_{sat}$	kN/m <sup>3</sup>	20	20	19

Reference secant stiffness for triaxle test	$E_{50}^{ref}$	kN/m <sup>2</sup>	13000	13000	34000
Tangent oedometer stiffness	$E_{oed}^{ref}$	kN/m <sup>2</sup>	13000	13000	34000
Unloading/reloading stiffness	$E_{ur}^{ref}$	kN/m <sup>2</sup>	39000	39000	102000
Power for stress level	m	–	0.5	0.5	1
Cohesion	$c_{ref}$	kN/m <sup>2</sup>	0	0	10
Friction angle	$\phi$	°	39	39	30
Dilatancy angle	$\psi$	°	9	9	0
Poisson's ratio	$\nu_{ur}^{(nu)}$	–	0.3	0.3	0.3
Interface strength	–	–	Manual	Rigid	Manual
Interface reduction factor	$R_{inter}$	–	0.67	1	0.67
$K_0$ determination	–	–	Automatic	Automatic	Automatic
Lateral earth pressure coefficient	$K_0$	–	0.3707	0.3707	0.5000
Over-consolidation ratio	$OCR$	–	1.000	1.000	1.000
Pre-overburden pressure	$POP$	–	0.000	0.000	0.000

Numerically calculated lateral earth pressure is compared with physical model test data as shown in Figure 3.13, for the wall with 0.6 m height and 6 cm base thickness. The model retaining wall is analyzed with 50kPa surcharge load. The retaining wall is modeled as linear-elastic isotropic material. In order compare which model will more represent soil material behavior, the foundation and backfill soil are modeled with both Mohr-Coulomb and Hardening Soil material model. To avoid numerical instability while using PLAXIS for cohesionless backfill soil instead of taking the value of cohesion zero, it was taken 1kN/m<sup>2</sup>.



**Figure 3.13.** Validation of numerical lateral earth pressure results with experimental study.

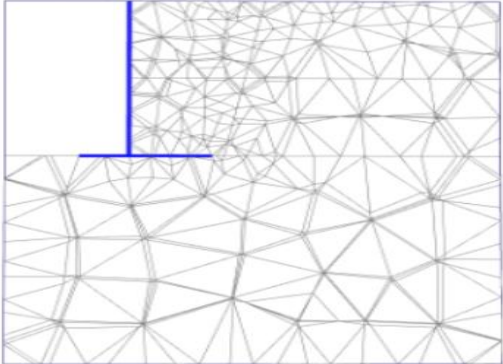
From the result both material models converge well with the experimental result but there is vertical discrepancy of numerical and experimental results, this discrepancy results from that, since the height of wall used in experimental model is 0.7 m but surcharge and backfill load applied at 0.1 m bellow top of wall or backfill thickness is 0.6 m. Hardening Soil is advanced model for simulating the behavior of different types of soil, both soft soils and stiff soils. So, in this investigation Hardening Soil model is better to represent the soil material model.

### 3.5. Convergence Analyses

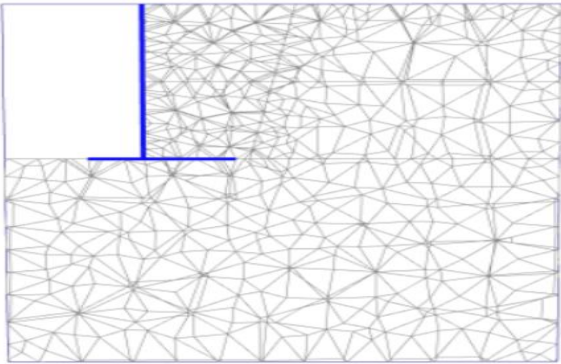
#### 3.5.1 Mesh Sensitivity Analysis

To access the accuracy of numerical results a convergence analysis was performed. Convergence analysis was carried out simulating the structure as a palate. Using PLAXIS 3D, four meshes of different density are considered namely; coarse, medium, fine and very fine (Figure 3.14). For all

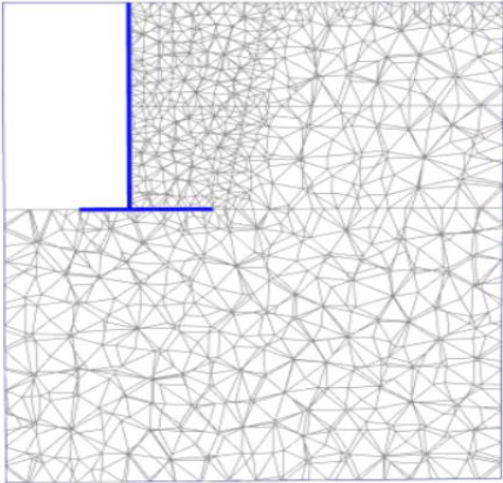
mesh cases local refinement was made on backfill near the retaining wall. As the mesh finesse become finer the calculation time and accuracy of the result increase.



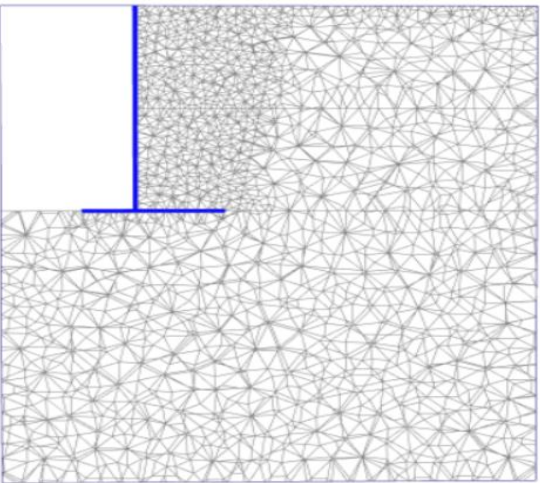
a. Coarse mesh



b. medium mesh

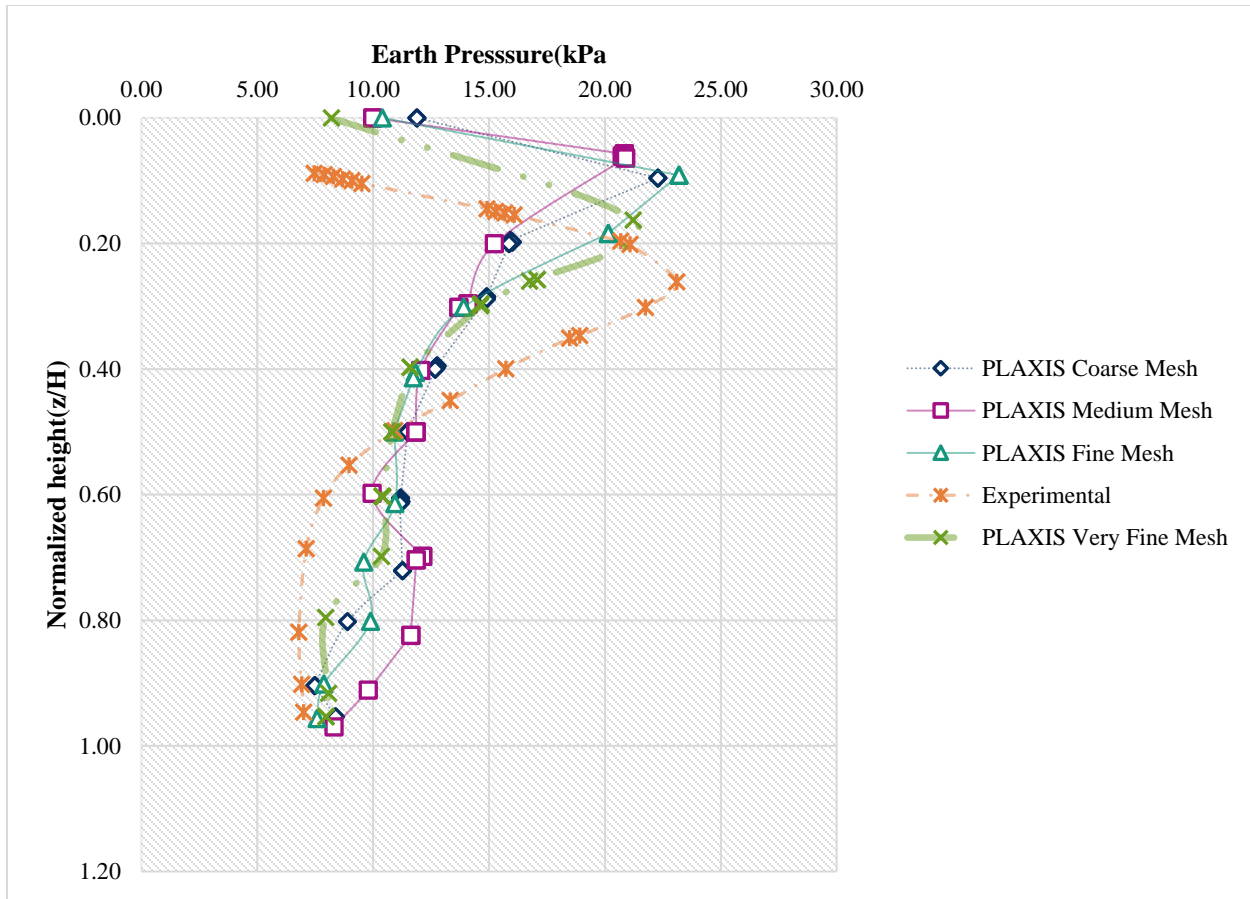


c. Fine mesh



d. Very fine mesh

**Figure 3.14.** Mesh finesse option.



**Figure 3.15.** Mesh convergence with lateral pressure distribution.

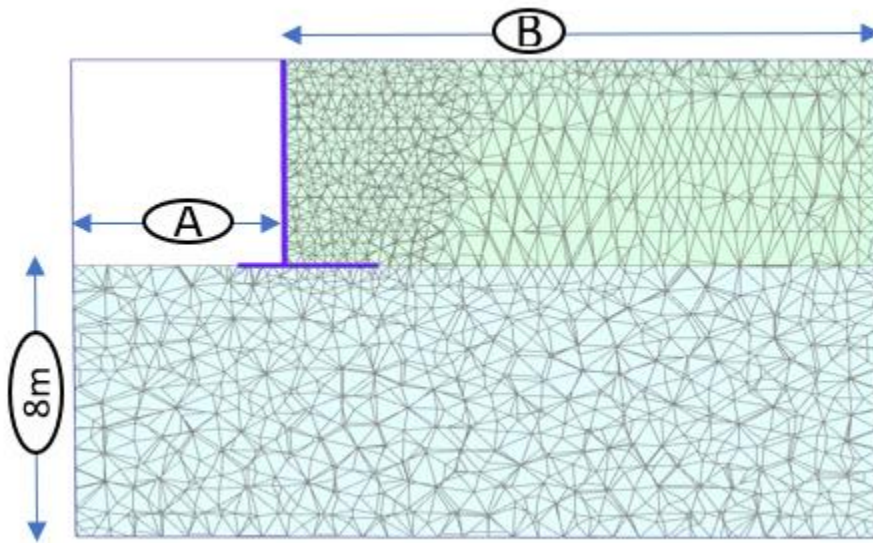
Based on the result it was clear that the mesh fines affect the lateral pressure distribution on the stem (Figure 3.15). However, as the mesh density increases some convergence observed, very fine mesh density converges best with the Experimental result. Considering these the mesh should be sufficiently fine to obtain accurate results, so the Very fine mesh used in PLAXIS to denote the highest level of mesh fines in this investigation.

### 3.5.2. Selection of Appropriate Finite Element Domain

In numerical analysis, it is important to eliminate the effect of the location of boundaries as much as possible in order to get a representative result. Although the boundary conditions recommended by the software were used for the simulation, it is necessary to determine the size of the simulation domain such that the computed responses are not affected by the selected boundary condition. To



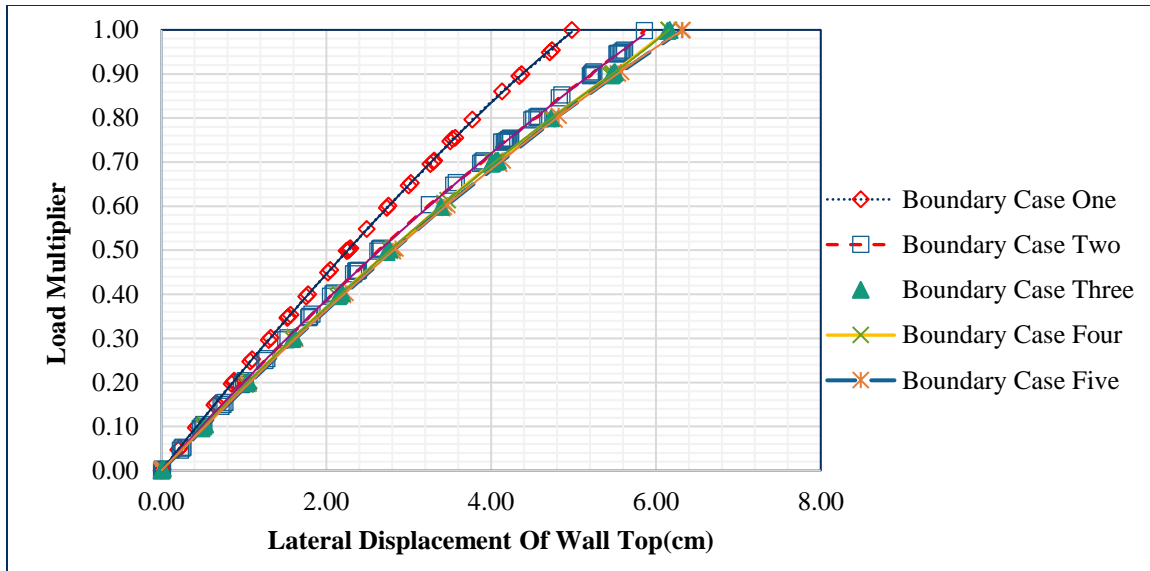
do this (Figure 3.16), using the Very Fine mesh previously selected, the width of the model was varied and the wall with 6 m height, 3.1 m length and with 3 m base width was used.



**Figure 3.16.** Mesh which shows various boundary limit A and B for size sensitivity analysis.

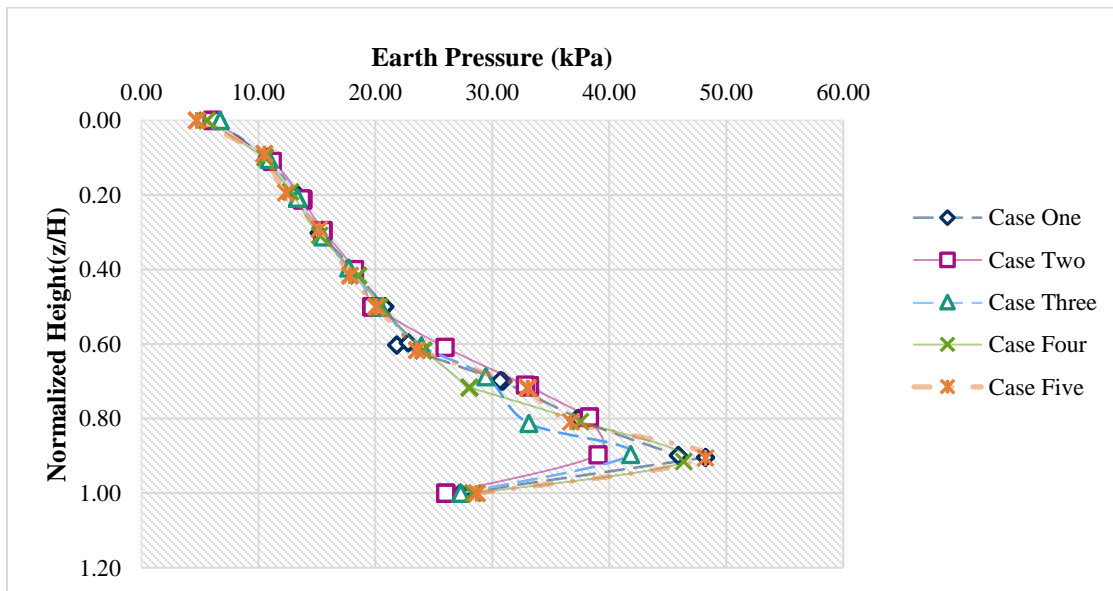
Five cases were considered that case one, where  $A=3$  m and  $B=9$  m, Case two where  $A=5$  m and  $B=11$  m, Case three where  $A=7$  m and  $B=13$  m, Case four where  $A=9$  m and  $B=15$  m and Case five where  $A=11$  m and  $B=17$  m.

The movement of the wall tip was a major consideration in determining the wall deflection, this was the first parameter to be observed. For each cases the wall tip displacement and lateral pressure distribution on the stem were observed. As shown in Figure 3.17, the displacement of wall tip for all considered boundary cases are presented.



**Figure 3.17.** Lateral displacement of wall tip at the end of Surcharge loading for all boundary cases.

Based on the results, it was clear that the model width has significant effect on the displacement of wall tip but as the dimension of the model size increases, best convergence has observed. However, three largest model sizes Case three, Case four and Case five converges well, boundary case four and five similarly rounds for wall tip displacement.

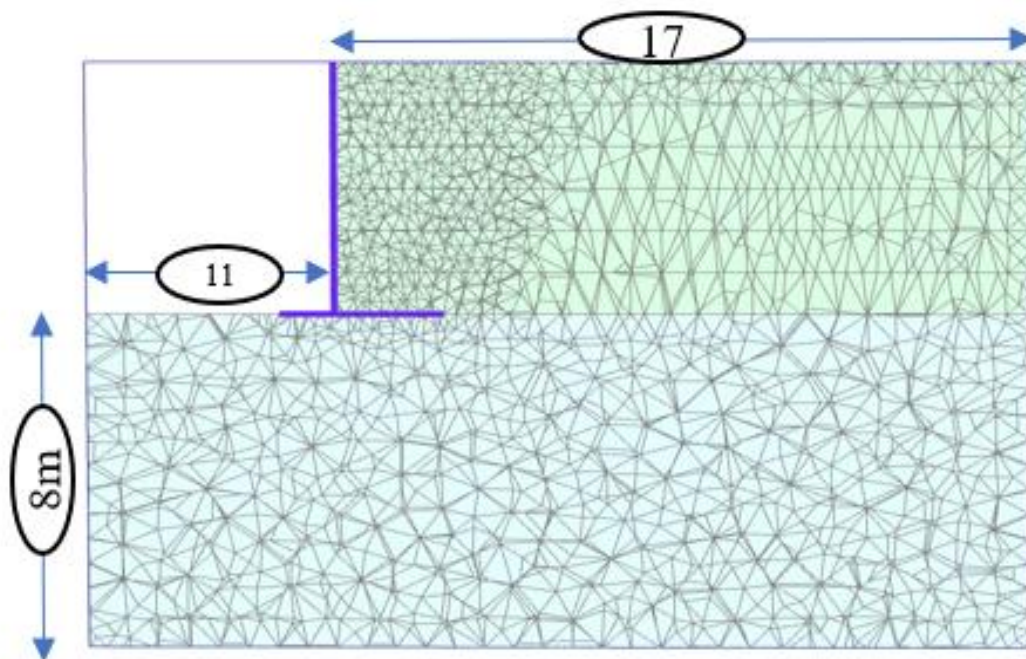


**Figure 3.18.** Lateral pressure distribution on the wall stem at the end of surcharge loading.

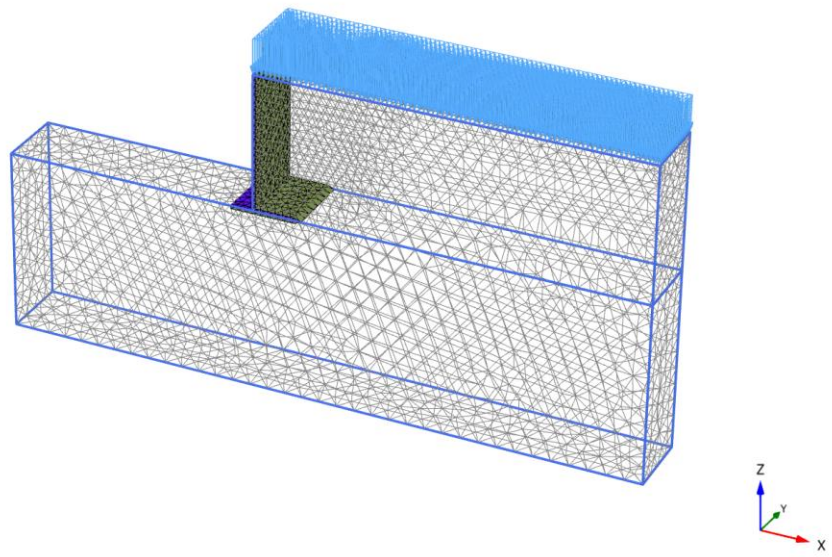
For consistency, the lateral earth pressure distribution on the wall stem were observed at the end of surcharge loading for each of model size and the results are shown in Figure 3.18. In case of lateral earth pressure distribution on the wall stem, the size of model does not appear to greatly affect the earth pressure distribution. Here the model size cause little change on the wall response but as the model size become larger the effect of boundary disturbance reduced. So, case 5 was suitable model for this thesis study

In case of computational time for calculation stage, boundary case five reduce the computational time compared to other boundary cases. So, boundary case 5 is suitable model for this thesis study since, a larger model will serve to reduce misleading effects of the boundary conditions and reduce computation time.

Based on the mesh sensitivity and size sensitivity analysis, the appropriate mesh fines and model size were determined. This, combination with the selected boundary conditions and retaining wall with different diminutions to be investigated in this study, was used to create basic finite element model that would be used for this study. In Figure 3.19, the configuration of finite element model used in this study depicted.



**Figure 3.19.** Finite element mesh model used in this study.



**Figure 3.20.** 3D representation of PLAXIS model used in this study.

# CHAPTER 4

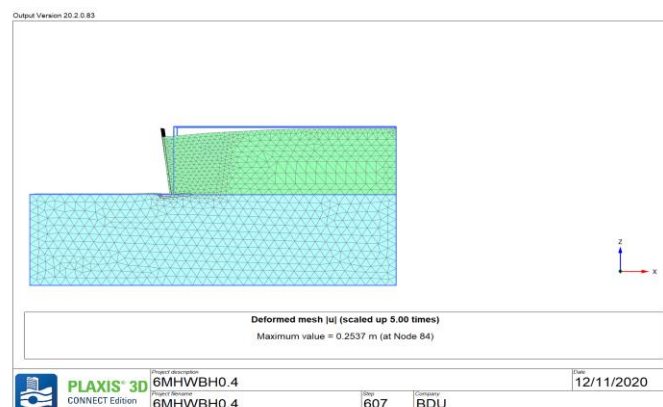
## 4. FINITE ELEMENT ANALYSIS RESULTS AND DISCUSSION

### 4.1. General

The numerical calculations are carried out for each wall separately, the calculation process starts from a stage of initial condition for different wall dimension. When the initial stress conditions are defined, the PLAXIS calculation program is loaded and the calculation process of stresses and displacements in the model is started, after completion of the calculation, the PLAXIS output generate the computed results. Prediction of displacements and forces are amongst the key objectives for performing soil-structure interaction analysis. The results of the present numerical analysis are presented mainly in terms of wall displacements and earth pressure computation. Brief indication of the predicted soil movement with wall displacement is discussed.

### 4.2. Soil Displacement

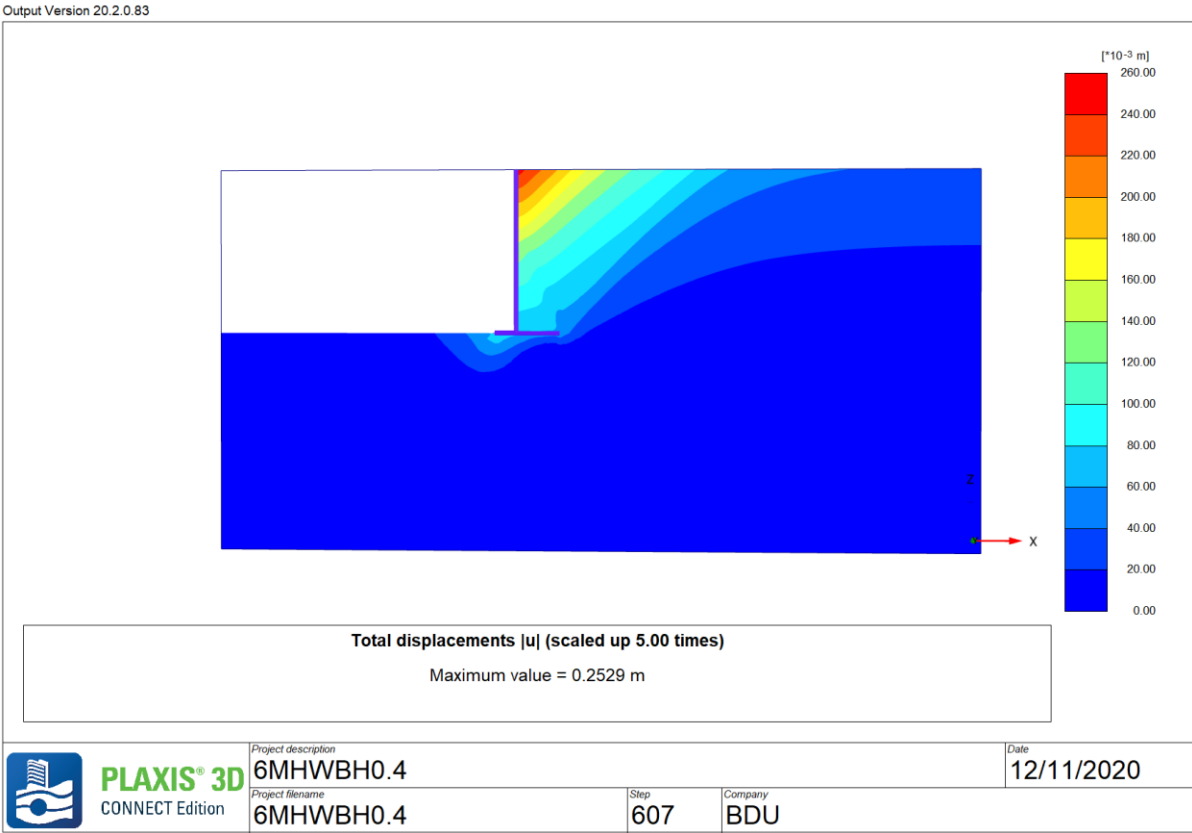
A typical post processing deformed meshes for the walls **6MHWB/H0.4** is presented in Figure 4.1 corresponding the state of end of surcharge loading. In this figure the displacement is scaled up 5 times to highlight the deformation pattern of wall (rigid body movement) and the soil mass.



**Figure 4.1.** Typical deformed mesh shows how much the nodes in the mesh moves.

In figure 4.1, the lateral support yields by tilting around its lower base and the horizontal surface of sand displaces. The soil displaces laterally and vertically following the movement of wall and this displacement more visible and higher at the top of the wall. After the support has yield sufficiently, active wedge faced following the surface of sliding which extends from the foot of the support (wall) to the surface of the sand as shown in Figure 4.2.

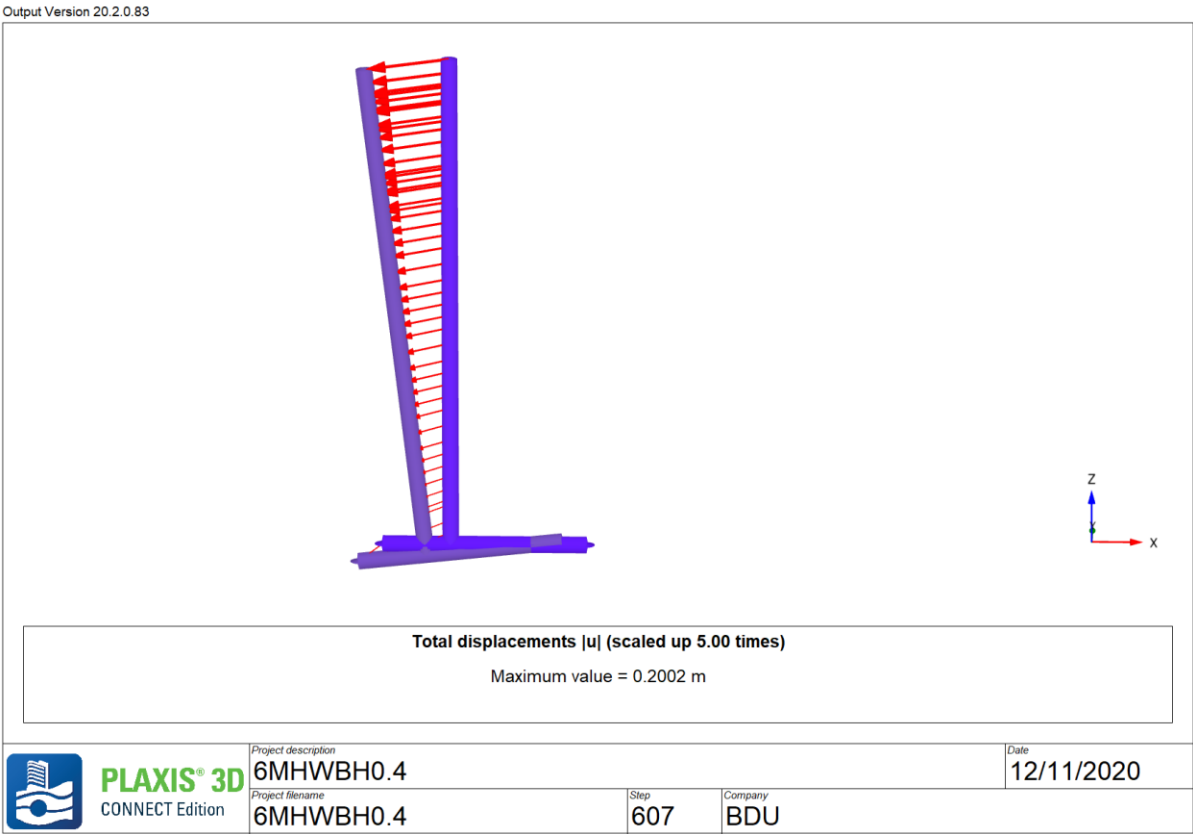
Figure 4.2 gives an indication of the total displacement contour of the soil predicted at the stage of surcharge loading. It could be noticed that during the backfilling and surcharge loading process of the wall, the soil mass is in an active state and is moving with the wall, also there were some concentration of displacement vectors beneath the wall base and inside the backfill part, this is in contradiction with the design practice of “T-shaped” retaining wall where, the soil mass resting on the wall base is assumed to be part of the wall, and its displacement is not taken in to account.



**Figure 4.2.** Total displacement vector of the soil representing the amount of soil displacement at the end of surcharge loading.

Following the movement of the wall, the soil mass displacement extends inside the backfill and to some extent beneath the base of the wall. As shown in Figure 4.3, the maximum displacement vectors of the soil mass appear at the tip (top) of wall and the minimum displacement vectors of soil mass appears beneath the wall base and it extends from foot to the surface of backfill. From the figure 4.3 the soil failure wedge starts at the heel of the base and extends to the backfill.

### 4.3. Wall Displacement

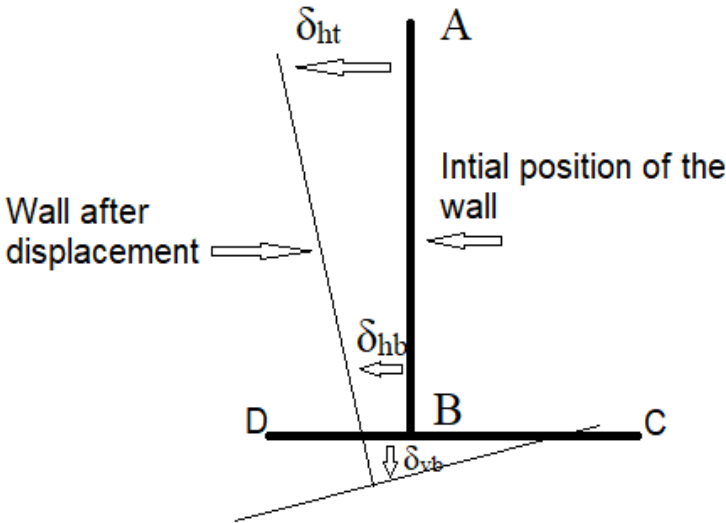


**Figure 4.3.** Total displacement vector of the wall shows direction and magnitude of displacement of the structure.

The resulting predicted total displacement vectors of the retaining wall is shown in Figure 4.4. It is clear that settlement of the wall was greater at the toe of the base. In addition to the forward tilt of the wall stem away from the original backfill, the base of the wall has also translated forward.

As a result, the computed wall movement by the proposed numerical model indicates a combination of rotation and translation. In most previous investigations, either pure rotation or translation was considered, but it is evident that both rotation and translation occur simultaneously, also, the centre of rotation is usually fixed either at the toe or the top of the wall, the numerical analysis confirms rotation takes place about an axis with in the relative displacement of stem top and bottom.

As illustrated in Figure 4.4,  $\delta_{ht}$ , represents the horizontal movement of wall at the top of the stem (displacement of point A);  $\delta_{hb}$  is the horizontal movement of wall at the bottom of the stem (horizontal displacement of points B, C and D);  $\delta_{hv}$  is the Vertical movement of wall at the bottom of the stem (nodal vertical displacement of the point A and B).



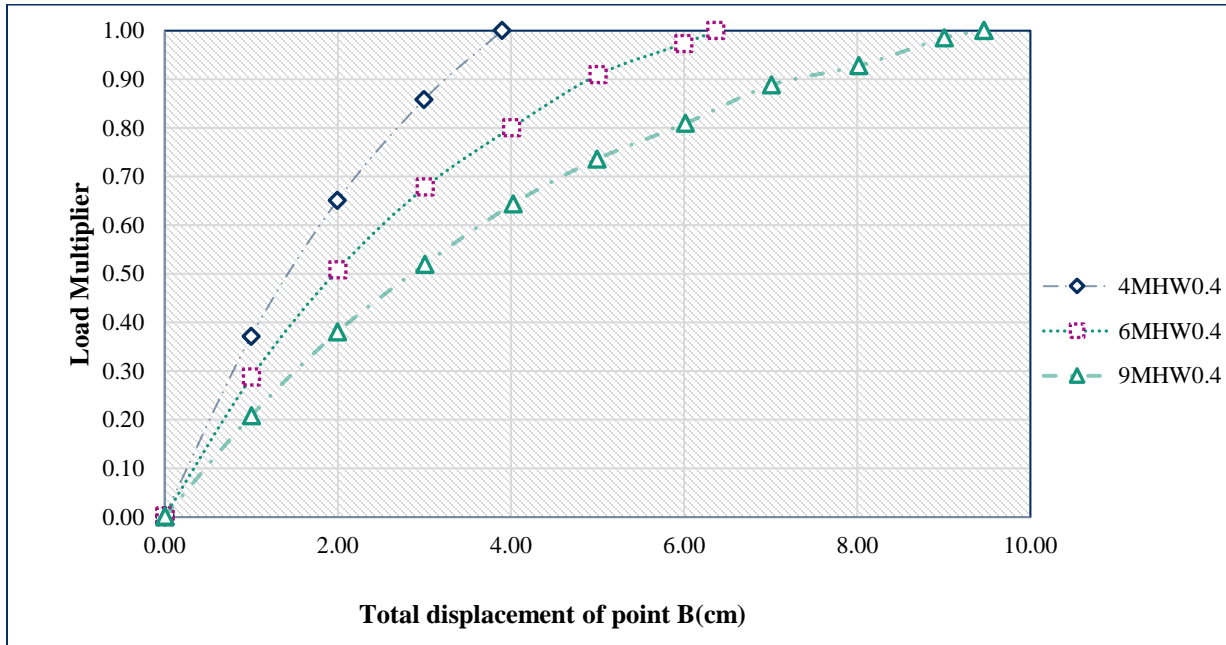
**Figure 4.4.** Nodal displacement pattern of the wall.

**4.3.1 The Effect of Wall Dimensions on The Mode of Wall Displacement**

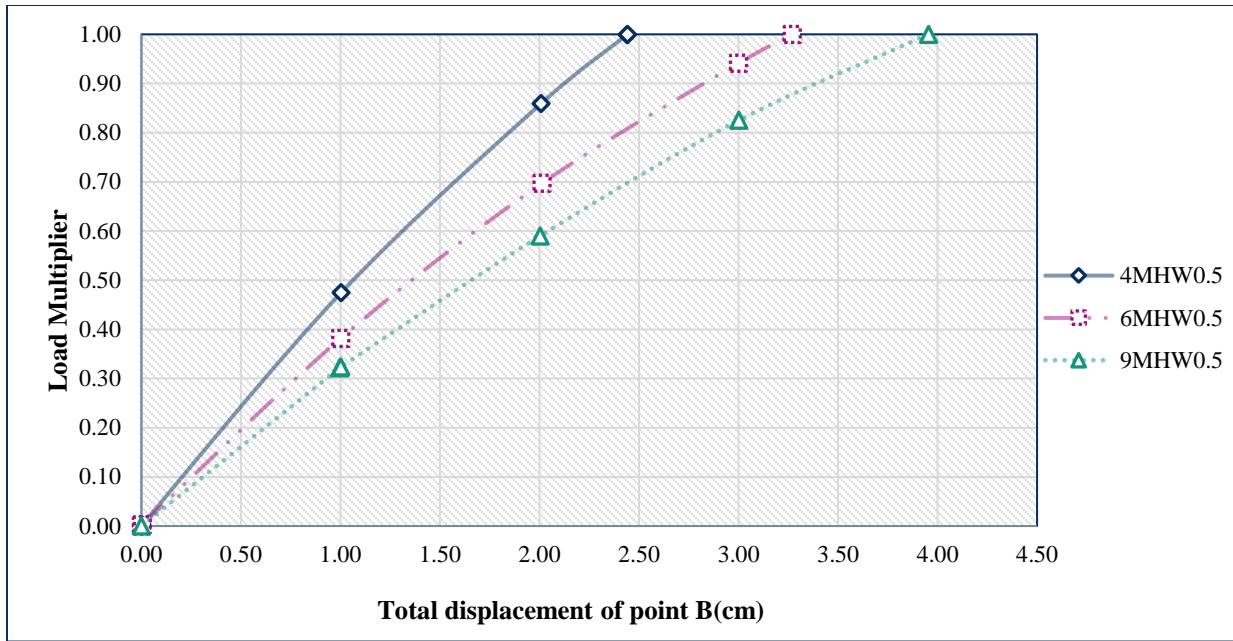
Figure 4.5 to Figure 4.8 shows, the computed nodal displacement of point B plotted against load multiplier, corresponding to different wall height with base to height ratio ranging from  $B/H = 0.4$  to  $B/H = 0.7$ . At the start of a staged construction calculation, the load multiplier that controls the staged construction process, is zero and this multiplier is stepwise increased to ultimate level



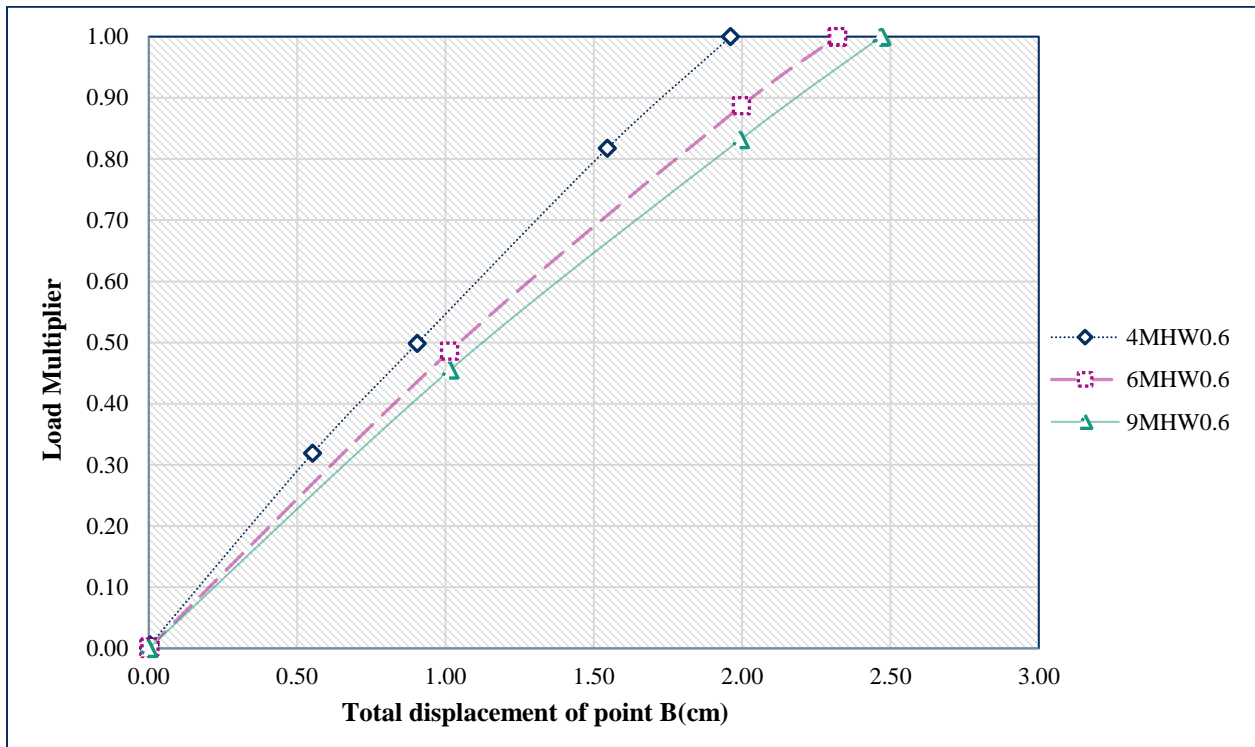
(generally 1.0). The load multiplier controls the out of balance force and the ultimate level of load multiplier 1.0 means the structure can with stand the loads higher than those we applied. When load multiplier has reached the ultimate level, the calculation phase is finished. However, if a staged construction calculation has not properly finished, i.e., the multiplier is less than the desired ultimate level at the end of a staged construction analysis, then a warning appears in the log info box.



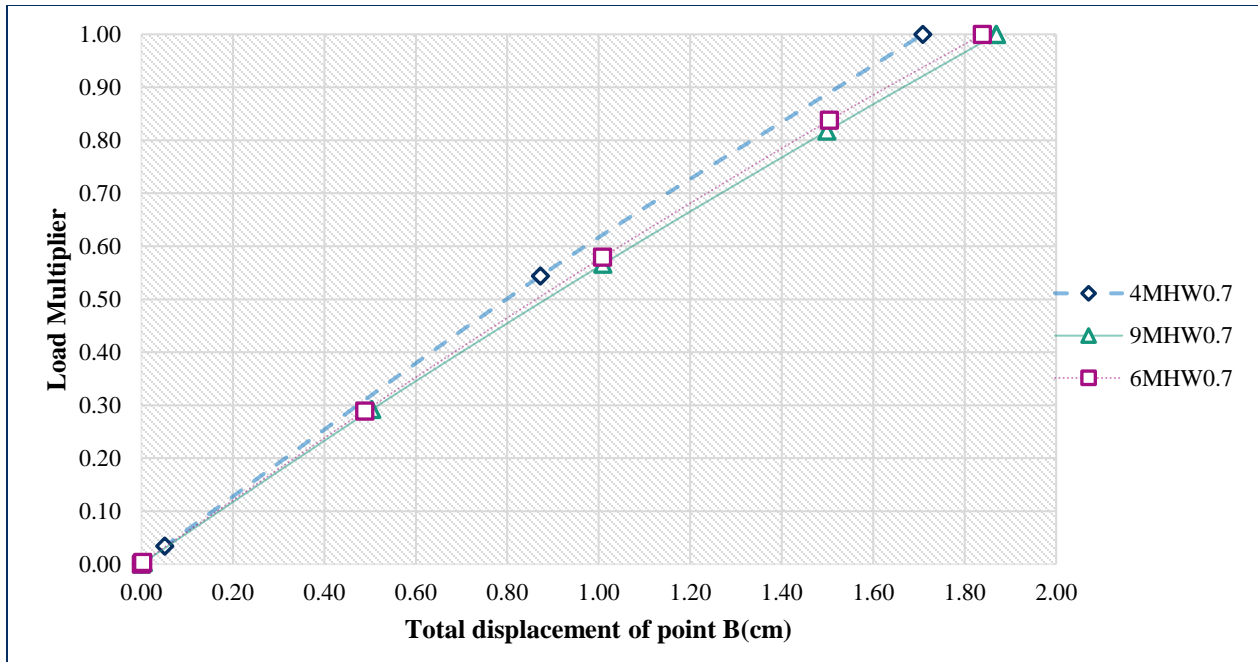
**Figure 4.5.** Total displacement of point B (B/H=0.4) considering different wall height.



**Figure 4.6.** Total displacement of point B (B/H=0.5) considering different wall height.



**Figure 4.7.** Total displacement of point B (B/H=0.6) considering different wall height.

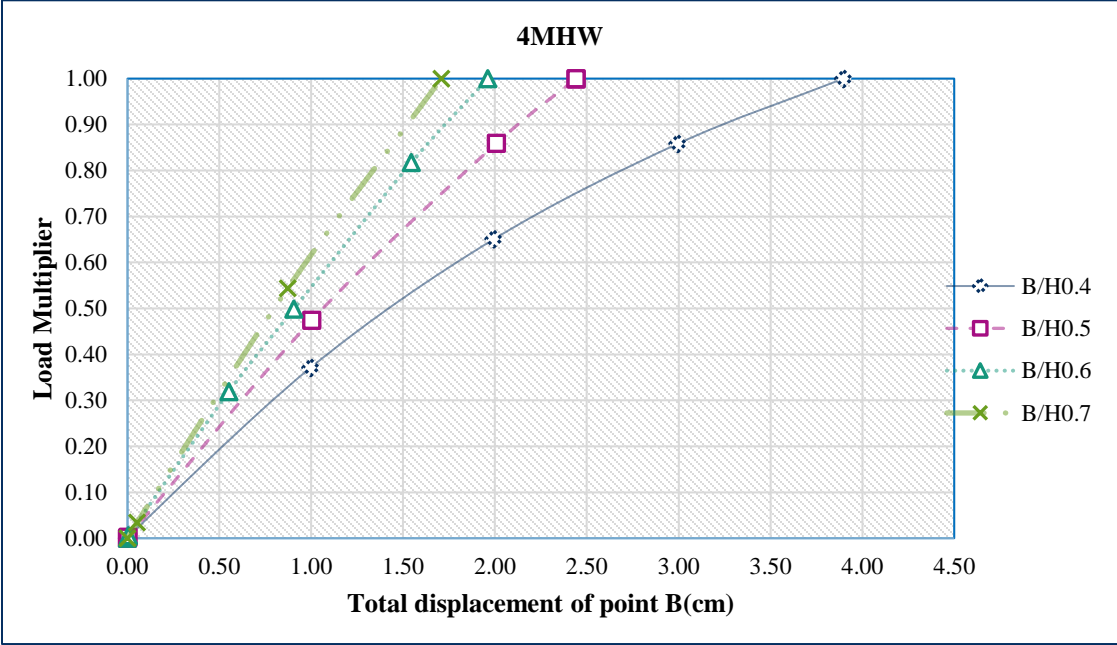


**Figure 4.8.** Total displacement of point B ( $B/H=0.7$ ) considering different wall height.

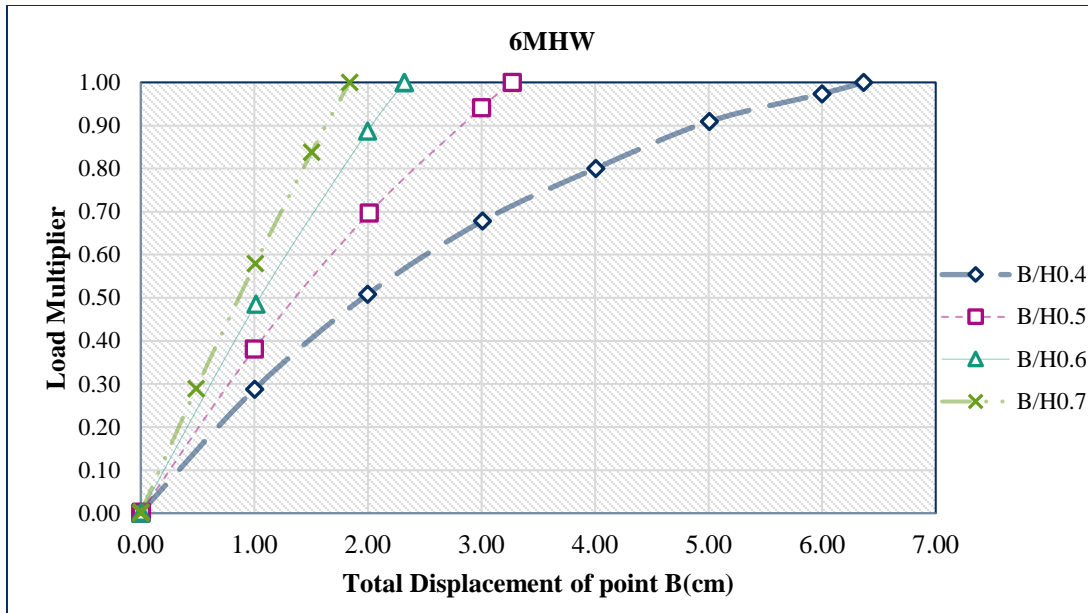
From these figures, it is clear that the displacement path corresponding to  $B/H = 0.4$  plotted in Figure 4.5 and the displacement path for  $B/H = 0.5$  plotted in Figure 4.6 follows curved lines which indicates the rotation effect, however, the displacement paths corresponding to  $B/H = 0.6$  plotted in Figure 4.7 and the displacement path for  $B/H = 0.7$  plotted in Figure 4.8 are closely linear which indicates the translation effect. Based on the results the displacement of wall at the bottom of the stem (nodal displacement of point B) increase following the increase of wall height for all base to height ratio.

Comparing the above series of figure, the pattern of the displacement curve is influenced by the value of base to height ratio ( $B/H$ ), for the wall with  $B/H=0.4$  and  $B/H=0.5$  as shown in Figure 4.5 and Figure 4.6 respectively, the displacement vector follows curved line and as the wall height increase the magnitude of displacement vector increase. For the wall with  $B/H=0.6$  and  $B/H=0.7$  as shown in Figure 4.7 and Figure 4.8, the displacement vector follows a linear pattern and there is closeness in magnitude of displacement as the wall height increase. Figure 4.8 depicted that, for the wall with 6m and 9m height the magnitude and pattern of displacement vector closer to one another other than wall with  $B/H = 0.4$  to 0.6 as shown in Figure 4.6 and Figure 4.7 respectively. This indicates that wall with large height and base width shows, closeness in magnitude and position (pattern) of displacement vector at the bottom of the steam.

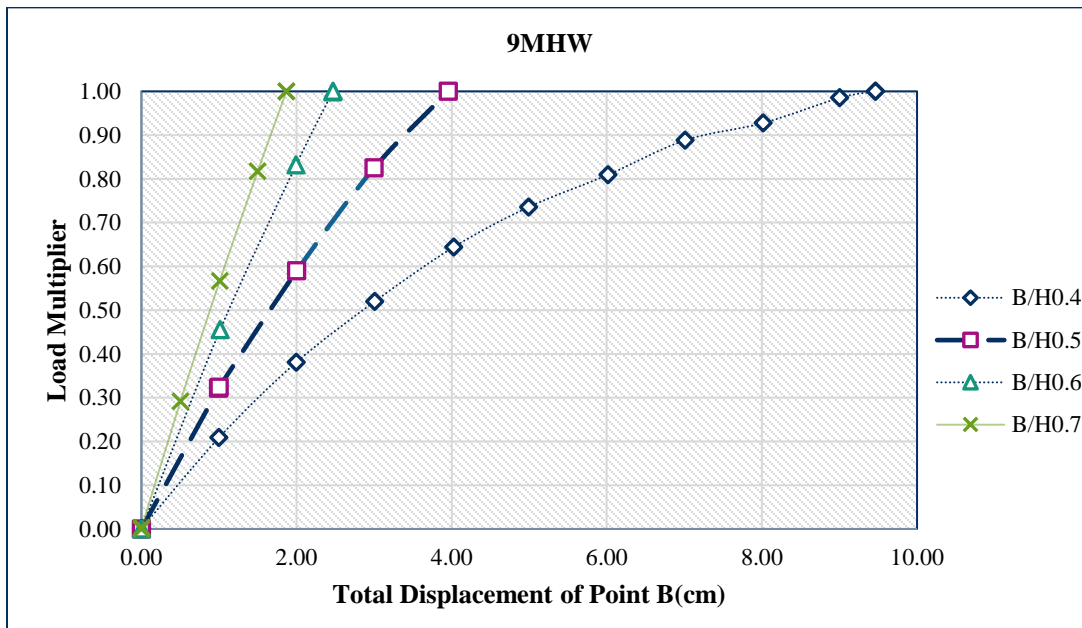
Figure 4.9 to Figure 4.11 shows the variation of displacement of wall at node B (bottom of the stem) considering height of the wall and base width to wall height ratio at the end of surcharge loading. From these figures the displacement of the wall, at the bottom of the stem (point B) decreases, as the ratio of base width to stem height ( $B/H$ ) increase for all 4m, 6m and 9m height walls.



**Figure 4.9:** Effect of base width to stem height ratio on total displacement of nodal point B (at the stem bottom) 4 m height wall.



**Figure 4.10:** Effect of base width to stem height ratio on total displacement of nodal point B (at the stem bottom) 6 m height wall



**Figure 4.11:** Effect of base width to stem height ratio on total displacement of nodal point B (at the stem bottom) 9 m height wall

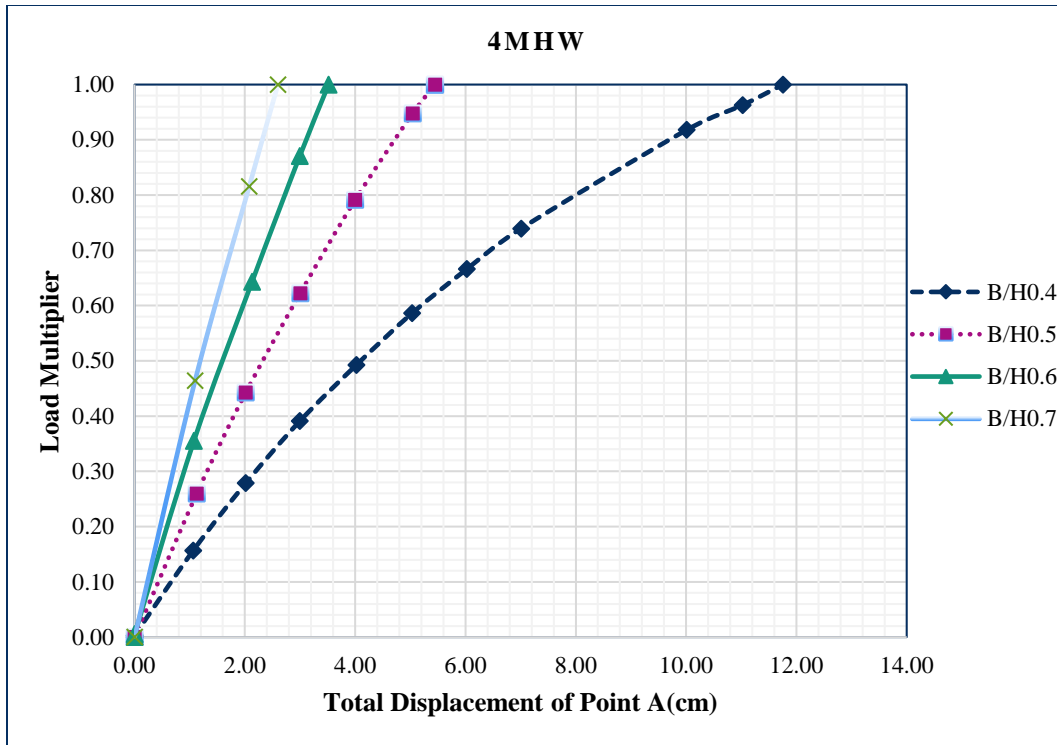
However, the displacement of the wall at the bottom of the stem (point B) decreases as the ratio of base width to stem height ( $B/H$ ) increase for all walls considered (Figure 4.9 to Figure 4.11), the

difference in magnitude of displacement vector for each consecutive base to stem height ratio increase with increasing wall height. But the effect of  $B/H = 0.4$  more visible in case of magnitude of displacement vector, since as the wall height increase the magnitude of displacement vector increase with higher difference. All walls i.e., 4m, 6m and 9m height with  $B/H = 0.7$ , the magnitude and pattern of nodal displacement closes better. Generally, for the wall with small height, the difference in displacement value for consecutive B/H ratios less and for the wall with large height, the difference in displacement value for consecutive B/H ratios are higher.

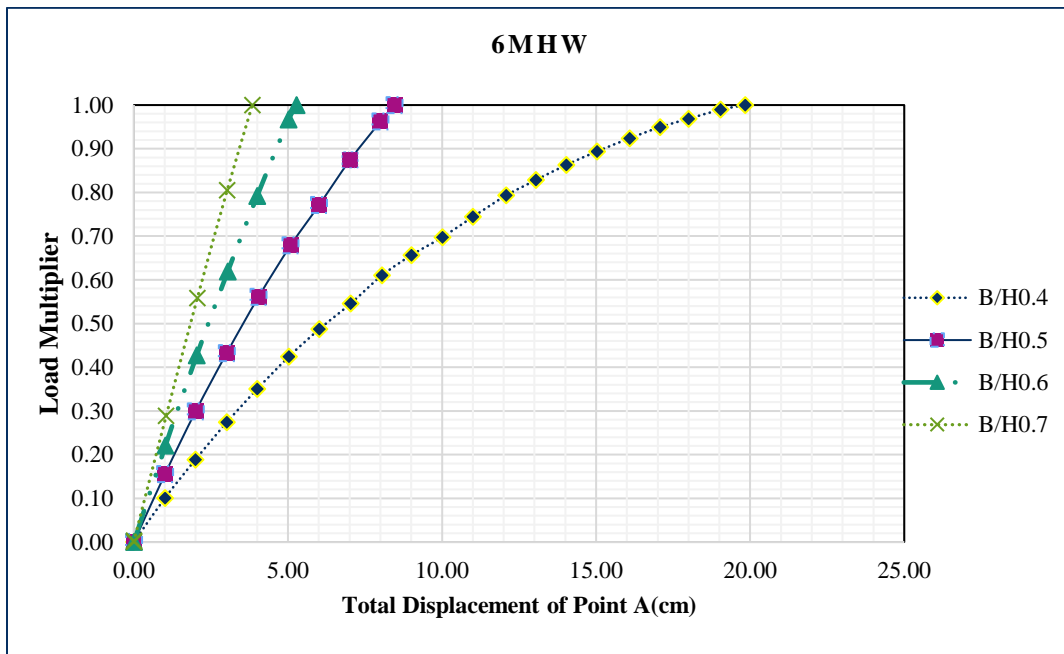
From these results, we can understand that, wall with smaller base width develops active earth pressure with in higher displacement limit and wall with larger base width develops active earth pressure in smaller displacement limit.

#### **4.3.4 The Effect of Base Width to Wall Height Ratio on Nodal Displacement of Point A**

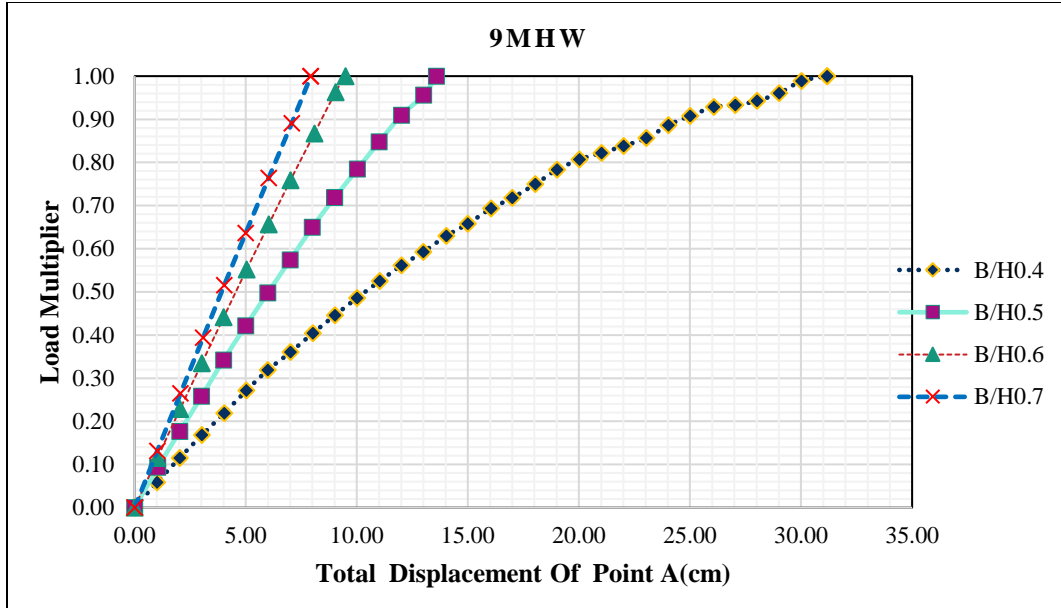
The displacement vector of wall stem tip is plotted against the loading stage multiplier in Figure 4.13 which shows, the variation of displacement of wall at node A (at top of the stem) considering height of the stem and base width to stem height ratio at the end of surcharge loading.



(a)



(b)



(c)

**Figure 4.12.** Effect of base width to stem height ratio on lateral displacement of nodal point A (at the stem top) for different wall height. (a). 4m height wall, (b). 6m height wall, (c). 9m height wall.

In figure 4.13(a), 4m height wall is illustrated. From the result the lateral displacement of the wall, at the top of the stem (point A) decreases, as the ratio of base width to stem height ratio ( $B/H$ ) increase. In Figure4.13(b), 6m height wall condition is depicted. According to this case, the lateral displacement of the wall, at the top of the stem (point A) decreases, as the ratio of base width to stem height ratio ( $B/H$ ) increase. In figure 4.13(c), 9m height wall is depicted. With similar fashion, the lateral displacement of the wall, at the top of the stem (point A) decreases, as the ratio of base width to stem height ratio ( $B/H$ ) increase. In comparison, the magnitude of lateral displacement of wall tip increase with increasing wall height for all  $B/H$  ratio considered. The incremental amount of lateral displacement of wall tip as the ratio( $B/H$ ) decrease for each consecutive ratio increase with increasing wall height.

Finally, the magnitude and pattern of wall displacement rounds similar where the ratio of  $B/H$  increase for all walls considered in this study. Comparing the two nodal displacements i.e., node point A (at the top of the wall) and node B (at the bottom of the wall), the amount of displacement



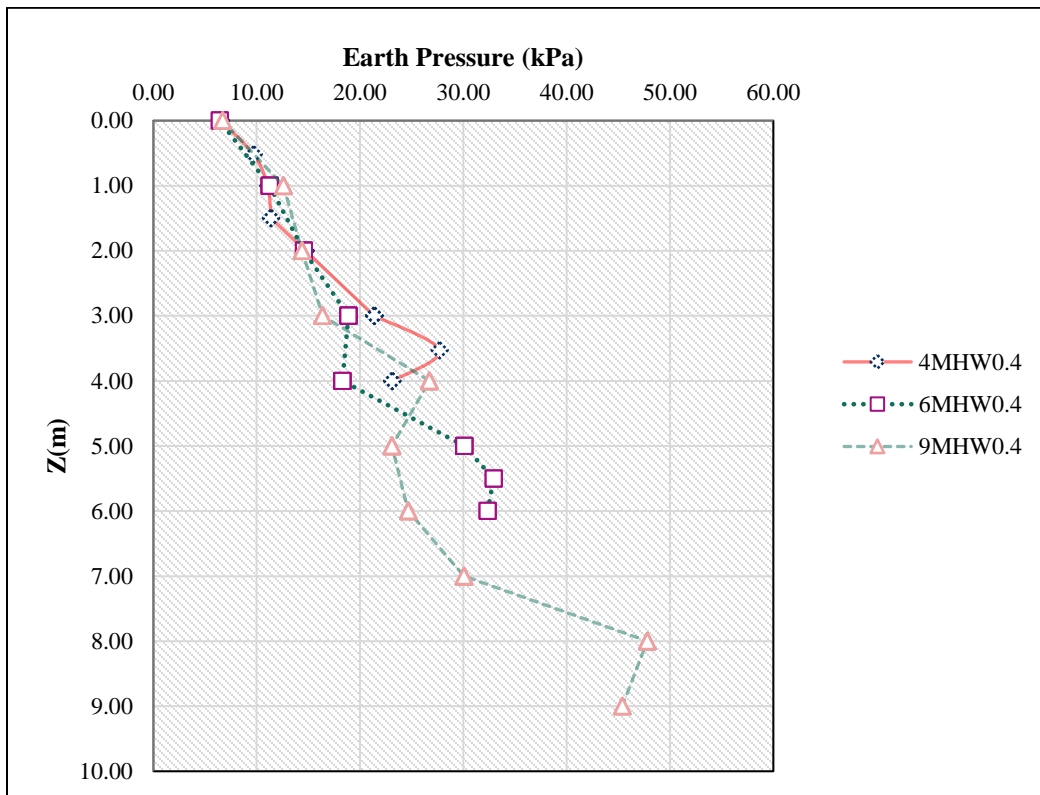
at the wall top is higher than the displacement at the bottom of the stem for all the wall considered in this study, this indicates that the wall tilts about its lower edge.

#### 4.4. Determination of Lateral Pressure Distribution

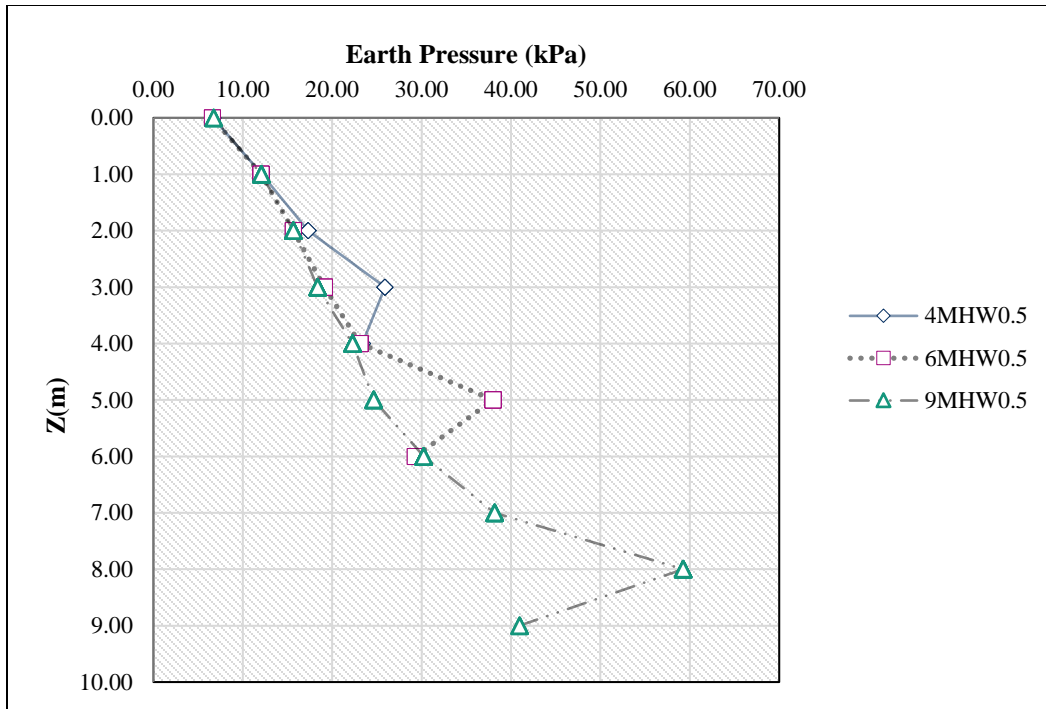
##### 4.4.1 The Effect of Wall Height on Lateral Earth Pressure Distribution Behind the wall

###### Stem

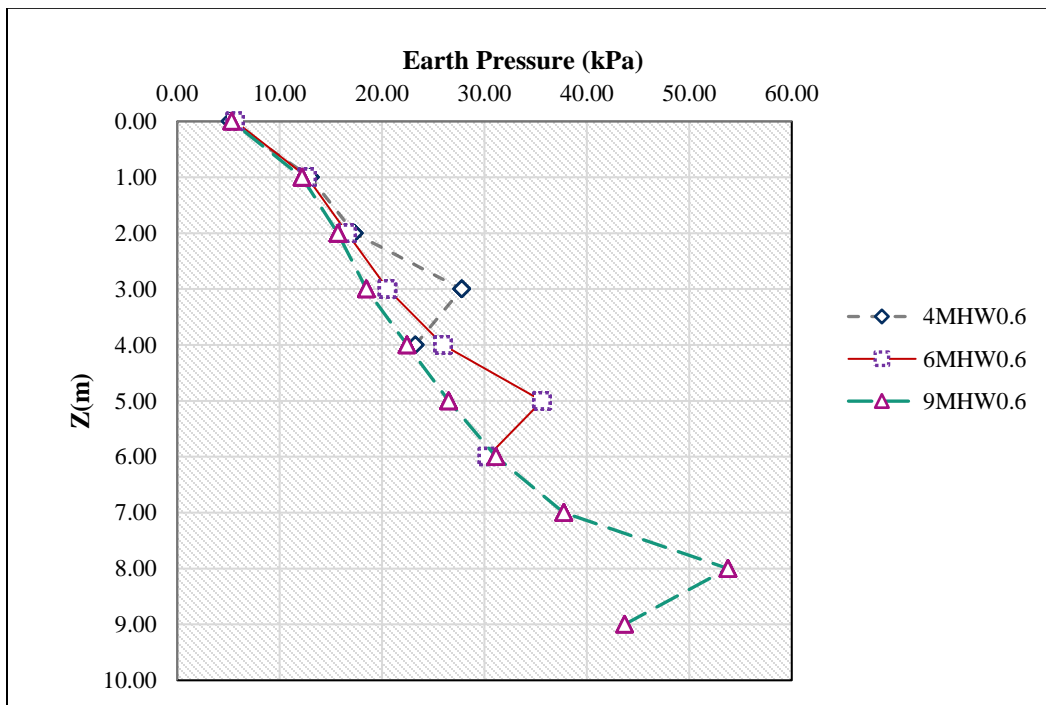
The active lateral earth pressure distribution acting on the stem of the retaining wall as a result of varying the wall height for different base width to stem height ratio are shown in Fig. 4.12. The stem of inverted T-shaped retaining wall was considered in the FE analysis to investigate the lateral earth pressure distribution. In order to ensure comparableness, the wall height for various base to height ratio ( $B/H$ ) of inverted T-shaped retaining walls taken into account.



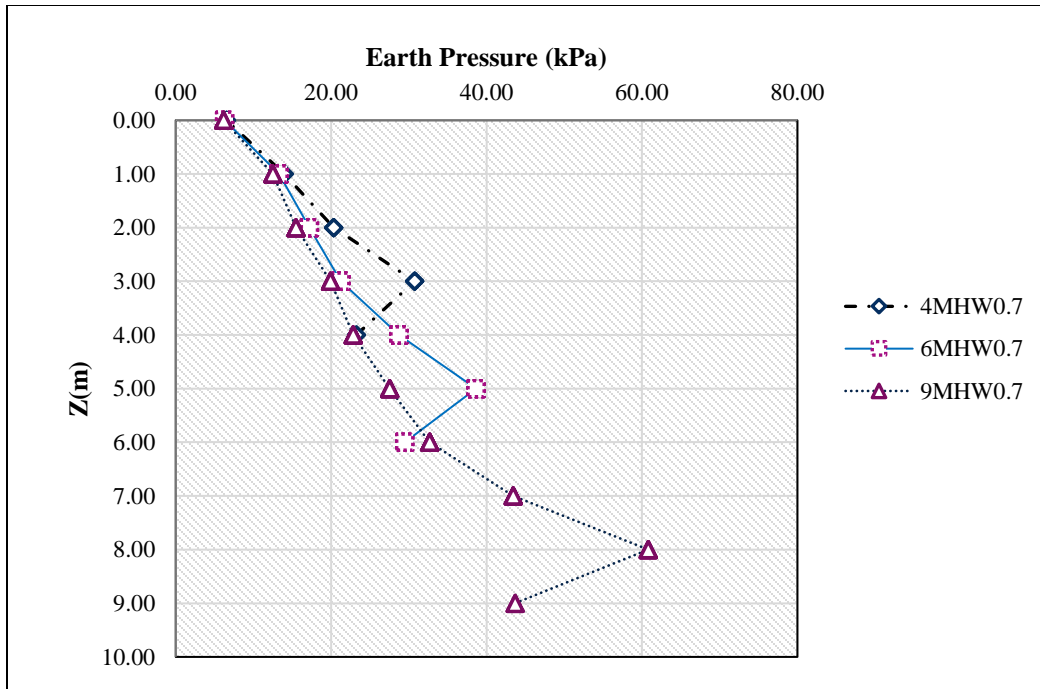
a.



b.



c.



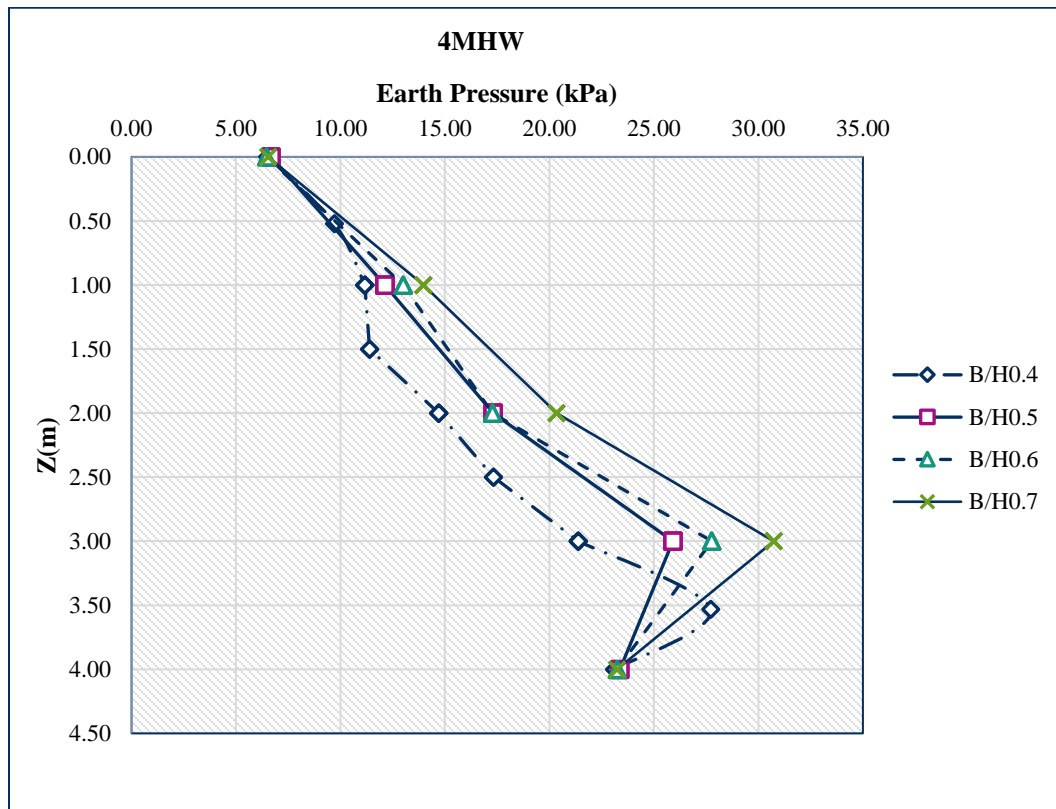
d.

**Figure 4.13.** Effect of wall height on lateral earth pressure distribution; (a). walls with  $B/H$  0.4, (b). walls with  $B/H$  0.5, (c). wall with  $B/H$  0.6, and (d). walls with  $B/H$  0.7.

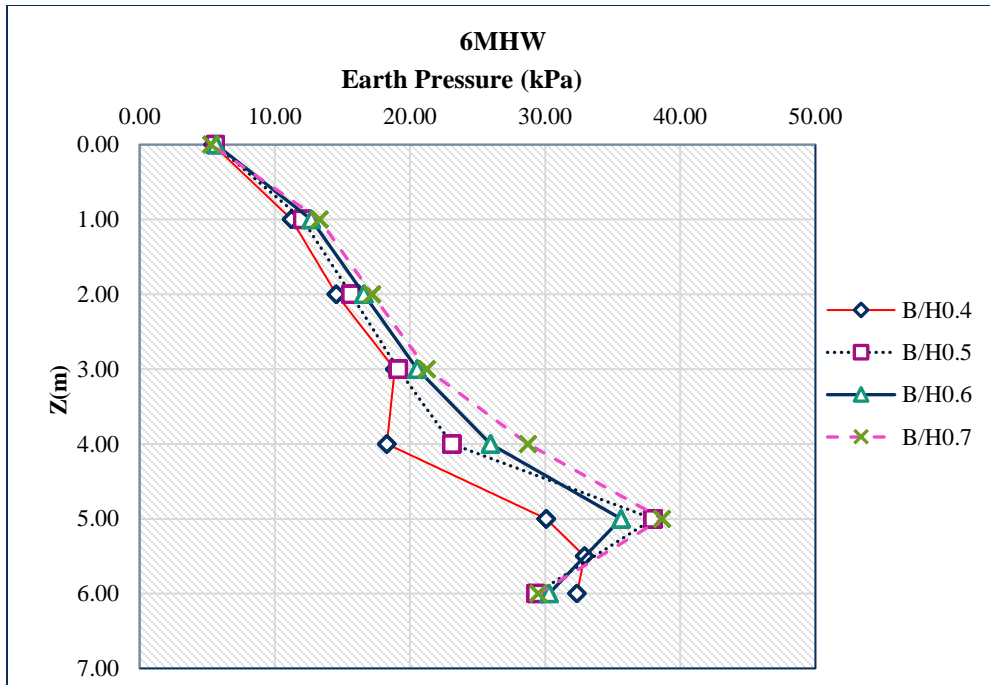
In figure 4.14(a) the computed lateral pressure for different wall height with base to wall height ratio( $B/H$ ) 0.4 depicted. In Figure 4.14(b) the computed lateral pressure for different walls with base to wall height ratio( $B/H$ ) 0.5 presented. In figure 4.14(c) and Figure 4.14(d) the computed lateral pressure for different wall height with base to wall height ratio( $B/H$ ) 0.6 and  $B/H$  0.7 depicted respectively. From these consecutive figures, it can be observed from the result that, at the beginning of depth of wall the distribution nature and magnitude of lateral earth pressure rounds similar with the same value of  $B/H$  ratio for all wall height considered, but as the depth increase the variation of magnitude of lateral earth pressure increase. However, the distribution nature of lateral earth pressure nearly the same. As it can be observed from the consecutive figures, the shapes of the distribution nature of lateral pressure are the same for different retaining wall heights which means that the height of the retaining wall does not have an effect on the shape of the lateral active earth pressure distribution.

#### 4.4.1 The Effect of Base Width to Wall Height Ratio on Lateral Earth Pressure Distribution

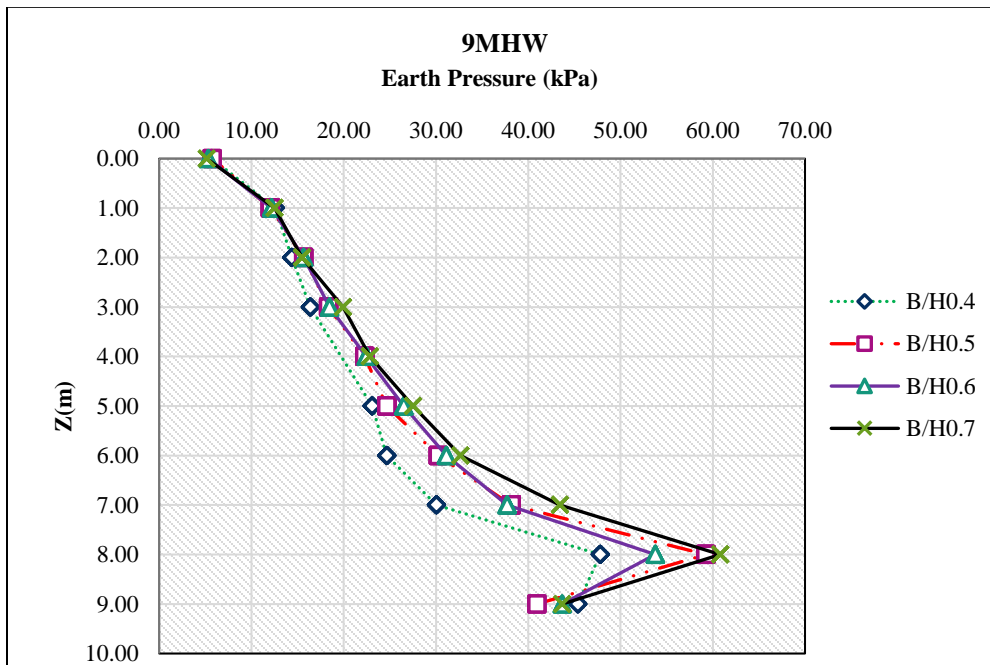
Figure 4.14, shows the lateral earth pressure profiles as a result of varying the base length to stem height ratio  $B/H$  on each wall height. From these figures it can be observed that the slope and magnitudes of the lateral pressures acting on different walls nearly comparable regardless the wall base to height ratio and magnitude of lateral pressure increase accordingly as the base width increase.



a.



b.



c.

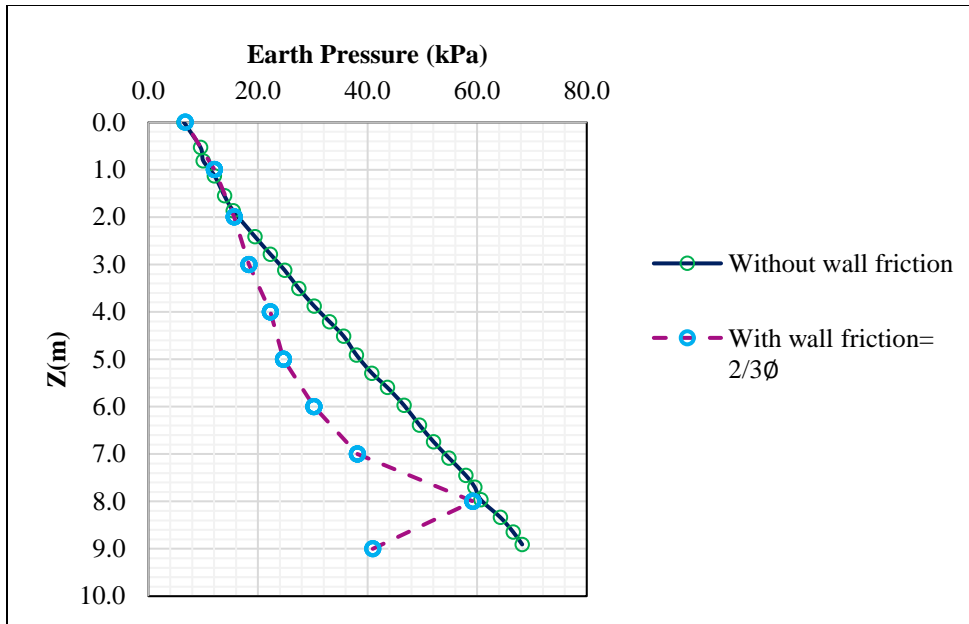
**Figure 4.14.** Effect of base width to height ratio on lateral earth pressure distribution, (a). lateral pressure variation for 4MHW, (b). lateral pressure variation for 6MHW, and (c). lateral pressure variation for 9MHW.

From the result it shows that, following increasing the ratio  $B/H$  for each wall, it could be noticed that the lateral pressure seems to increase accordingly and there is a gap in distribution pattern of earth pressure between consecutive ratios, this effect will be results from, the relative pressure applied from surcharge load and the weight of the backfill soil resting on the wall base. In this study, as far as the distribution of lateral pressure acting on the wall stem concerned, the distribution of lateral pressure from the result of numerical analysis is non-linear but it contradicts with the practical design approach (linear distribution) applied for inverted T-shaped wall. On the Figures 4.14, around one meter from the bottom of the wall height, there is abrupt change with decreasing value of lateral pressure(slope), this is common for all walls considered. It could be argued that the distribution nature of the lateral pressure change depends on the height of the wall and seems not influenced by the base length.

In comparison, for the wall with 9m height in figure 4.14(c) there is similarity in distribution nature (slope) and magnitude of lateral pressure for the consecutive ratios, rather 4 m height wall and 6 m height wall as illustrated in figure 4.14(b) and figure 4.14(c) respectively for all base width considered. Hence, for the wall with larger height, the distribution nature and magnitude of the lateral pressure rounds well similar for the consecutive base width considered.

#### **4.4.2 Checking Arching Effect on Lateral Active Earth Pressure Distribution on The Wall Stem**

Arching effect results from the transfer of pressure from a yielding mass of soil onto the adjoining stationary parts when part of a yielding support moves out more than the adjoining parts. Since all numerically computed results of lateral earth pressure distribution presented in the above section were examined by considering wall friction  $2/3\phi$ . So, to check the occurrence of the arching effect on the distribution nature of lateral active earth pressure behind the stem, 9 m height wall with and without wall friction tested and the results presented in Figure 4.15.



**Figure 4.15.** Lateral active earth pressure distribution with and without wall friction behind the stem.

From the result the nature of lateral earth pressure distribution with out wall friction follows linear line. According to this case, the retaining wall does not carry any shear stress since there is no wall backfill friction, due to this no transfer of pressure from a yielding mass of soil onto the adjoining stationary parts and it cause no arching.

Generally, in design practice the lateral pressure distribution is assumed to be linear. However, it is clear that the non-linearity of the lateral pressure profile is apparent in numerically computed results. This result proves the study of Fang and Ishibashi (as cited in Ertuğrul, 2013), that based on the results of experimental studies it was observed that pressure distribution against translating and rigid retaining walls are significantly non-linear due to soil arching. The distribution nature of active earth pressure obtained for walls supporting backfill sand can be attributed to arching effect development in the backfill. The trajectory of lateral earth pressure distribution direction shows an inverted arch about one meter from the bottom of the wall base. Additionally, small lateral pressure at the lower elevation of the backfill near the wall were observed for all the wall considered. The numerical result further proves the theoretical work on soil arching introduced by Karl Terzaghi (1943).

# CHAPTER 5

## 5.1. CONCLUSION

In this research, the effect of different wall dimensions on lateral earth pressure distribution and displacement pattern of wall at the stem bottom and tip of the wall were evaluated numerically using PLAXIS 3D. Within this scope, an inverted T-shaped retaining walls with 4 m, 6 m and 9 m height wall and base to height ratio( $B/H$ ) ranging from 0.4 to 0.7 considered. From these results, it shows that the proportioning governs the equilibrium between the instantaneous rotation and the translation effect of wall at the bottom of the stem. Substantial findings of the study are summarized as follow;

1. For the value of base width to wall height ratio less than or equal to 0.5 the rotational effect of displacement pattern dominant. However, for the value of base width to wall height ratio greater than and equal to 0.6 the translational effect of displacement pattern governs. So, the preliminary geometric ratio ranging from 0.4 to 0.7 remains reasonable as far as the equilibrium between the rotation and translation of the wall concerned and practically, these ranges of preliminary  $B/H$  ratio results for safe and economical design of retaining structures.
2. Following the increasing of wall height, the nodal displacement of wall at the stem bottom and top increase for all case of  $B/H$  ratio.
3. Generally, for all cases of wall heights, as the ratio of  $B/H$  increase the displacement of wall at the bottom and top of stem decrease. Hence, as the base width increase the vertical pressure on the footing increase stability of wall, that may the cause wall with larger base width has smaller displacement.
4. Wall with smaller base width develops active earth pressure with in higher displacement limit and wall with larger base width develops active earth pressure in smaller displacement limit.
5. As increasing the ratio of  $B/H$  for each wall, it could be noticed that the lateral pressure seems to increase accordingly for all the walls considered. The distribution nature of lateral earth pressure is non-linear upon the numerical method used in this study and there is slope change around one meter from the bottom of stem with decreasing magnitude of earth pressure, this is due to arching effect. This effect results, since numerical computation considers rough wall-



backfill interface and frictional forces occur along the wall-backfill interface along which shear stress can be carried within the retained material by enabling lateral arching.

Finally, this study will contribute for researchers interested in solving problems related to the design of different retaining structures. The study will fill the gap on designing safe and economical retaining walls by calculating the displacement limit and considering the nonlinear nature of lateral earth pressure distribution which results from arching effect.

## **Recommendations for Future Work**

In terms of reliability analysis, further study is recommended to improve the distribution nature of lateral earth pressure. In practice, retaining walls designed only by checking stability against different failures, but the displacement limit to develop lateral pressure and nonlinear distribution nature of lateral pressure does not take in to account. So, designer should calculate the displacement limit and check the nonlinear nature of lateral pressure.

## REFERENCES

1. Ahmed Rouili (2013). "Design of Rigid L- Shaped Retaining Walls." J. Civil and Environmental Engineering Vol:7, No:12,  
<https://www.researchgate.net/publication/259217120>
2. A. Rouili, Y. Djerbib, M. Touahmia. (2005). "Numerical modelling of an L shaped very stiff concrete retaining wall." J. Civil and Environmental Engineering (3).
3. Antonello Di Sotto, Salvatore Miliziano (2014). "Criteria for Numerical Modelling of Very Stiff Cantilever Retaining Structures." Article in Rivista Italiana di Geotecnica. September 2014 <https://www.researchgate.net/publication/26705536>.
4. Bushra S. Albusoda, Hassan Obaid Abbas and Safa Hussain Abid Awn (2017). "Numerical Modeling of Retaining Wall Resting on Expansive Soil." Geotechnical Engineering Journal of the SEAGS & AGSSEA Vol. 48 No. 4 December 2017 ISSN 0046-5828,  
<https://www.researchgate.net/publication/321384443>
5. Chia-Cheng and Fan Yung (2010). "Numerical solution of active earth pressures on rigid retaining walls built near rock faces." J. Computers and Geotechnics Vol.37, pp. 1023–1029, [www.elsevier.com/locate/comgeo](http://www.elsevier.com/locate/comgeo).
6. Craig, R. F. (2004). Craig's soil mechanics. 7th ed. New York. Spon Press.
7. Dahunsi B.I.O, Adewuyi A.P. And S. I Adedokun (2015). "Modelling of the structural behaviors of cantilever retaining wall." NSE Technical Transaction Vol 49, No 1, <https://www.researchgate.net/publication/333843917>
8. Eleanor Lynn huggins (2012). "Numerical and Reliability Analysis of Gravity Cantilever Retaining Walls Backfilled with Shredded Tires Subjected to Seismic Loads." [https://tigerprints.clemson.edu/all\\_theses/1437](https://tigerprints.clemson.edu/all_theses/1437)
9. Ersan Yildiz (2003). Lateral Pressures on Rigid Retaining Walls.
10. Firas A. Salman, Yousif J. Al-Shakarchi, Husain M. Husain and Dunya K. Sabre (2010). "Distribution of earth pressure behind retaining walls considering different approaches." International Journal of the Physical Sciences Vol. 5(9), pp. 1389-1400.
11. Hakan Alper Kamiloglu and Erol Sadoglu (2019). "Numerical Analysis of Active Earth Pressures on Inverted T Type and Semi-Gravity Walls." Int. Conference on Advanced Engineering Technologies (3), <https://www.researchgate.net/publication/335950849>

12. Hetham A. Ramadan Amer (2013). “Effect of Wall Penetration Depth on The Behavior of Sheet Pile Walls.” Master thesis, May, 2013.
13. H.J. Lengkeek (2003). “Estimation of sand stiffness parameters from cone resistance.” J. Computer and Geotechnics, <https://www.researchgate.net/publication/332043192>.
14. J. Devid Rogers (1986). “Determination of Earth Pressure Distributions for Large-Scale Retention Structures.” Article August 1986, <https://www.researchgate.net/publication/266275308>.
15. José Medina, Nicolás Sau and Jesús Quintana (2016). “Lateral Displacement of Retaining Walls.” Journal of Geological Resource and Engineering 6 (2016) 251-256 <https://www.researchgate.net/publication/311527510>.
16. Joseph E. Bowles (1996) Foundation Analysis and Design -5th Ed.
17. Karl Terzaghi (1943). Theoretical soil mechanics, arch in ideal soils, Ninth Printing.
18. Mathias Pettersson, (2012). “In depth study of lateral earth pressure, A comparison between hand calculations and PLAXIS.” J. Geotechnical Engineering Research Group, Master’s Thesis 2012:69
19. Minoru Matsuo, Satoru Kenmochi and Hideki Yagi (1978). “Experimental study on earth pressure of retaining wall by field tests.” Japan’s society of soil mechanics and foundation engineering, soil and foundations Vol. 18, No.3.
20. Nihan Aydin Ertuğrul (2013). “Effect of soil arching on lateral soil pressures acting upon rigid retaining walls.” Master’s Thesis 2013:61
21. N. Phien-wej, M. Humza and Z. Zaw Aye:” Numerical modeling of diaphragm wall behavior in Bangkok soil using hardening soil model.” International Society for Soil Mechanics and Geotechnical Engineering (ISSMGE), Taylor & Francis Group, London, ISBN 978-0-415-68367-8, <https://www.issmge.org/publications/online-library>
22. Plaxis 3D Reference manual, Material Models and Tutorial Manual Connect edition v20.
23. Reza Darbana & Farzin Kalantary (2015). “Lateral Pressure on Rigid Retaining Walls without Lateral Movement.” J. Computational Research Progress in Applied Science & Engineering, ISSN 2423-4591.
24. Rizwan Khan, Vinay Bhushan Chauhan and Satyanarayana Murty Dasaka (2016). “Reduction of lateral earth pressure on retaining wall using relief shelf: A numerical study:” Conference Paper, July 2016, <https://www.researchgate.net/publication/305719594>

25. Sneha Rachel Cherian and Jiss K Abraham (2018). “Numerical Modelling and Analysis of Retaining Wall with Crumb Rubber as Backfill.” International Research Journal of Engineering and Technology (IRJET), Vol. 05, e-ISSN: 2395-0056.
26. T. Schanz, P.A. Vermeer and P.G. Bonnier (1999). “The Hardening Soil Model: Formulation and Verification.” Beyond 2000 in Computational Geotechnics – 10 years of PLAXIS, Balkema.
27. Yao Tang, Jing Pei Li, and Yuan Ma. (2018). “Lateral Earth Pressure Considering the Displacement of a Rigid Retaining Wall.” Int. J. Geomech., 2018, 18(11): 0601803, <https://www.researchgate.net/publication/327465823>
28. Yap Soon Poh and Sharif Moniruzzaman Shirazi (2012). “Comparative Study of Different Theories on Active Earth Pressure.” Journal of Central South University of Technology, DOI: 10.1007/s11771-012-1361-2, <https://www.researchgate.net/publication/236694077>
29. Yi Tang and Jiangong Chen (2018). “A Computational Method of Active Earth Pressure from Finite Soil Body.” Mathematical Problems in Engineering Volume 2018, Article ID 9892376, 7 pages.
30. Wojciench Solowski (2017). “Numerical methods in geotechnics.” Geo-E2020.